

THE STELLAR CUSP AROUND THE SUPERMASSIVE BLACK HOLE IN THE GALACTIC CENTER

R. GENZEL,¹ R. SCHÖDEL, T. OTT, F. EISENHAEUER, R. HOFMANN, AND M. LEHNERT
 Max-Planck-Institut für extraterrestrische Physik, Postfach 1312, Garching D-85741, Germany

A. ECKART

1. Physikalische Institut, Universität Köln, Cologne, Germany

T. ALEXANDER

Faculty of Physics, Weizmann Institute of Science, Rehovot, Israel

A. STERNBERG

School of Physics and Astronomy, Tel Aviv University, Ramat Aviv, Israel

R. LENZEN

Max-Planck-Institut für Astronomie, Heidelberg, Germany

Y. CLÉNET, F. LACOMBE, AND D. ROUAN

Observatoire de Paris-Meudon, Meudon, France

AND

A. RENZINI AND L. E. TACCONI-GARMAN

European Southern Observatory, Garching, Germany

Received 2003 February 26; accepted 2003 May 23

ABSTRACT

We analyze deep near-IR adaptive optics imaging (taken with NAOS/CONICA on the Very Large Telescope at the European Southern Observatory, Chile), as well as new proper-motion data of the nuclear star cluster of the Milky Way. The surface density distribution of faint ($H \leq 20$, $K_s \leq 19$) stars peaks within $0''.2$ of the black hole candidate Sgr A*. The radial density distribution of this stellar “cusp” follows a power law of exponent $\alpha \sim 1.3$ – 1.4 . The K -band luminosity function of the overall nuclear stellar cluster (within $9''$ of Sgr A*) resembles that of the large-scale Galactic bulge but shows an excess of stars at $K_s \leq 14$. It fits population synthesis models of an old, metal-rich stellar population with a contribution from young, early, and late-type stars at the bright end. In contrast, the cusp within $\leq 1''.5$ of Sgr A* appears to have a featureless luminosity function, suggesting that old, low-mass, horizontal-branch/red-clump stars are lacking. Likewise, there appear to be fewer late-type giants. The innermost cusp also contains a group of moderately bright, early-type stars that are tightly bound to the black hole. We interpret these results as evidence that the stellar properties change significantly from the outer cluster (\geq a few arcseconds) to the dense innermost region around the black hole. We find that most of the massive early-type stars at distances of $1''$ – $10''$ from Sgr A* are located in two rotating and geometrically thin disks. These disks are inclined at large angles and counter-rotate with respect to each other. Their stellar content is essentially the same, indicating that they formed at the same time. We conclude that of the possible formation scenarios for these massive stars the most probable one is that 5–8 million years ago two clouds fell into the center, collided, were shock compressed, and then formed two rotating (accretion) disks orbiting the central black hole. For the OB stars in the central arcsecond, on the other hand, a stellar merger model is the most appealing explanation. These stars may thus be “super-blue stragglers,” formed and “rejuvenated” through mergers of lower mass stars in the very dense ($\geq 10^8 M_\odot \text{ pc}^{-3}$) environment of the cusp. The “collider model” also accounts for the lack of giants within the central few arcseconds. The star closest to Sgr A* in 2002, S2, exhibits a $3.8 \mu\text{m}$ excess. We propose that the mid-IR emission comes either from the accretion flow around the black hole itself or from dust in the accretion flow that is heated by the ultraviolet emission of S2.

Subject headings: black hole physics — galaxies: nuclei — Galaxy: center — stars: formation

1. INTRODUCTION

Because of its proximity (distance 8 kpc; Reid 1993), the center of the Milky Way is a unique laboratory for studying the physical processes in galactic nuclei (e.g., Genzel, Hollenbach, & Townes 1994; Morris & Serabyn 1996; Mezger, Duschl, & Zylka 1996; Melia & Falcke 2001). In particular, the Galactic center offers the unique opportunity for investigating stars and gas in the immediate vicinity of a

supermassive black hole, at a level of detail that will not be accessible in any other galactic nucleus in the foreseeable future. In the present paper we present and analyze new high-resolution adaptive optics (AO) imaging and observations of stellar velocities in the nuclear cluster, relating to its spatial distribution, evolution, and dynamics. Let us summarize what is known from observations during the past decade.

First, the overall surface density and surface brightness of stars increases with decreasing separation from the center near the compact radio source Sgr A* (diameter ~ 10 lt-minutes; Doeleman et al. 2001), with a near-isothermal

¹ Also Department of Physics, University of California, Berkeley, CA 94720.

power law (stellar volume density $\propto R^{-2}$) from projected radii $p \leq 100''$ to about $10''$ (Catchpole, Whitelock, & Glass 1990). Within that radius the surface brightness continues to increase inward to $1''$, but the stellar surface number density at moderately bright magnitudes ($K \leq 15$)² flattens, consistent with a half-peak surface brightness/density (core) radius of $\sim 0.34 \pm 0.2$ pc (Genzel et al. 1996). The value of the core radius is uncertain. The lower limit comes from surface density counts of the brightest few hundred stars (Eckart et al. 1993). The upper limit comes from the surface brightness distribution of late-type stars (Allen 1994) and measurements of the integrated light of faint stars in between the brightest stars (Rieke & Rieke 1994). The largest concentration of $K \leq 13$ stellar light and surface density is not centered on Sgr A* but on the IRS 16 complex about $2''$ east of it. This offset has been interpreted as evidence that Sgr A* cannot be a massive black hole (e.g., Allen & Sanders 1986).

Second, there are several different stellar populations/components in the central parsec (for a review see Genzel 2001). The stellar mass and the near-IR light at $K \geq 13$ is dominated by red giants in the old (1–10 Gyr) component of the nuclear star cluster. A group of about a dozen luminous blue supergiants (“He I emission-line stars”) strongly affects the near-IR maps at the bright end ($K \sim 9$ –12) and probably indicates recent formation of massive stars within the last 2–7 Myr (Forrest et al. 1987; Allen, Hyland, & Hillier 1990; Krabbe et al. 1991, 1995; Tamblyn et al. 1996; Blum, Sellgren, & DePoy 1996b; Paumard et al. 2001). A number of bright ($K \sim 10$ –12) asymptotic giant branch (AGB) stars sample an intermediate-mass, intermediate-age component (≥ 100 Myr; Lebofsky & Rieke 1987; Krabbe et al. 1995; Blum et al. 1996b). Finally, there is a group of dust-embedded stars with nearly featureless near-IR spectra (Becklin et al. 1978; Krabbe et al. 1995; Genzel et al. 1996), many of which are associated with the gaseous minispiral (Lo & Claussen 1983). Their nature is uncertain. The near-IR luminosity function to $K \leq 16$ resembles that of the Galactic bulge in Baade’s window (Blum, Sellgren, & DePoy 1996a; Davidge et al. 1997; Alexander & Sternberg 1999).

Third, the mean stellar velocities (or velocity dispersions) follow a Kepler law ($\langle v^2 \rangle \propto R^{-1}$) from ~ 0.1 to $\geq 20''$ and provide compelling evidence for the presence of a central compact mass (Genzel et al. 1996, 1997, 2000; Eckart & Genzel 1996, 1997; Ghez et al. 1998). Overall, the stellar velocities are consistent with an isotropic velocity field, but the He I emission-line stars appear to be preferentially on tangential orbits (Genzel et al. 2000). Statistical modeling of the stellar velocity data (projected mass estimators, Jeans equation modeling, nonparametric modeling) imply that the $(2\text{--}3.3) \times 10^6 M_\odot$ central dark mass is concentrated on scales less than 10 lt-days (Eckart & Genzel 1996, 1997; Ghez et al. 1998, 2000; Genzel et al. 2000; Chakrabarti & Saha 2001; Eckart et al. 2002). Most recently, Schödel et al. (2002, 2003) and Ghez et al. (2003) found that the star closest to Sgr A* in 2002, S2, is on a highly elliptical Keplerian orbit around the radio source. The enclosed mass within the orbit’s pericenter approach of 17 lt-hr (in 2002 April, at which point the star had a sky projected velocity of ≥ 5000

km s^{−1}) is $(3.5 \pm 0.5) \times 10^6 M_\odot$ (Schödel et al. 2003), which is within the uncertainties the same as the mass at distances of 10 to several hundred light days. As a result, the density of a hypothetical, non-black hole configuration has to have a central density of $2 \times 10^{17} M_\odot \text{ pc}^{-3}$ or greater. When combined with the 8–20 km s^{−1} upper limit to the proper motion of Sgr A* (Backer & Sramek 1999; Reid et al. 1999, 2003a) and a theoretical analysis of the motion of a black hole in the central star cluster, the density limit increases to $\geq 10^{19.5} M_\odot \text{ pc}^{-3}$ (Schödel et al. 2003). The new orbital data now definitely exclude a dark cluster of astrophysical objects (e.g., neutron stars) or a ball of 10–60 keV fermions as possible configurations of the central mass concentration. The only non-black hole configuration is a ball of hypothetical, heavy bosons, which would not be stable, however. The gravitational potential in the central light year of the Galactic center thus is almost certainly dominated by a massive black hole associated with Sgr A*.

We would like to better determine the distribution, properties, and dynamics of the different stellar components and understand their formation and evolution. We need to sample the numerous lower mass stars in the nuclear star cluster to determine the overall stellar density distribution and centroid. Theory predicts a number of effects that are unique to the environment of a black hole (for a review see Alexander 2002). There should be a density “singularity” of the star cluster (a “stellar cusp”) centered on the hole (Bahcall & Wolf 1976, 1977; Young 1980). Because of the very dense environment, close encounters and direct stellar collisions can occur and alter the stellar distribution, dynamics, and population near the hole. Giant stars can be destroyed (Davies & Benz 1991; Rasio & Shapiro 1990; Davies et al. 1998; Alexander 1999) and exotic stars created (e.g., Thorne & Zytlow 1975). Given the extensive evidence for hot, massive stars in the central parsec, we need to answer how they came into being in the very dense central environment. We also would like to detect Sgr A* itself in the near-/mid-IR and place tighter constraints on the accretion flow properties (Melia & Falcke 2001). We address all these issues in the present paper.

Previous data sets from the 3.5 m ESO New Technology Telescope (NTT; Eckart & Genzel 1996, 1997; Genzel et al. 1997, 2000), the 3.6 m Canada-France-Hawaii telescope (Davidge et al. 1997), and from the 10 m Keck telescope (Ghez et al. 1998, 2000) have FWHM resolutions of $0''.15$, $0''.16$, and $0''.05$, respectively, and reach to $K \leq 16$ –17. Deeper imaging at the diffraction-limited resolution of 8–10 m class telescopes is critical for addressing the problems outlined above. For this purpose we have carried out deep near-infrared AO observations with the new NAOS/CONICA instrument on the ESO Very Large Telescope (VLT; Lenzen et al. 1998; Rousset et al. 1998; Brandner et al. 2002). These observations provide diffraction-limited images at H ($1.65 \mu\text{m}$) and K_s ($2.16 \mu\text{m}$) to ~ 20 and at L' ($3.76 \mu\text{m}$) to ~ 14 . These improvements are largely due to the near-infrared wave front sensor of NAOS (which can lock on the bright star IRS 7 within a few arcseconds of Sgr A*) and the fact that the Galactic center passes through the zenith at Paranal. As a result, NAOS/CONICA achieves diffraction-limited imaging with stable and high (40%–50%) K -band Strehl ratios. Proper motions and radial velocities for about 1000 stars are now available from a new analysis of the ESO-NTT proper motions and integral field spectroscopy between 1992 and 2003 (T. Ott et al. 2003, in preparation). We

² Characteristic of main-sequence stars earlier than B0 and giants later than K4.

combine the AO observations with the new database of stellar proper motions and radial velocities, for a new analysis of the properties of the nuclear star cluster.

2. OBSERVATIONS AND DATA REDUCTION

The observations presented in this paper were carried out during science verification with the NAOS/CONICA AO system/near-infrared camera at the unit telescope 4 (Yepun) of the ESO VLT in Paranal, Chile. H -band ($1.65\ \mu\text{m}$), K_s -band ($2.16\ \mu\text{m}$), and L' -band ($3.76\ \mu\text{m}$) imaging data were taken on 2002 August 29. Seeing was between $0''.5$ and $0''.6$. For H and K_s the infrared wave front sensor of NAOS was used to close the feedback loop on the bright supergiant IRS 7 $\sim 5''.5$ north of Sgr A*. The detector pixel scale was $0''.0132\ \text{pixel}^{-1}$ for H and K_s and $0''.027\ \text{pixel}^{-1}$ for L' . The diffraction-limited resolution was 40, 55, and 95 mas in the H , K_s , and L' bands (FWHM). The oversampling helped to reduce the saturation of the numerous bright sources in the nuclear cluster. The detector integration time was 15 s. Four individual exposures were combined by a pipeline into one image of 60 s integration time. Twenty-five such images were taken in the H band and 20 in the K_s band. The individual images were flat-fielded, sky-subtracted, and corrected for dead/bad pixels. The final frames were co-added with a simple shift-and-add (SSA) algorithm to final images of 1200 s (K_s band; Fig. 1) and 1500 s (H band; Fig. 2) total integration time. The Strehl ratio measured on individual sources near the guiding star is $\sim 50\%$ in the K_s band and $\sim 33\%$ in the H band. Dithering between the exposures resulted in a field of view (FOV) larger than the $14'' \times 14''$ provided by CONICA with the finest pixel scale. From the

final mosaic we selected a $\sim 9'' \times 9''$ region with the highest signal-to-noise ratio, approximately centered on Sgr A*. There are numerous (~ 40 – 50) bright ($K_s < 12$) stars in the FOV, which are strongly saturated in the K_s -band image. Saturation is less severe in the H -band image. For L' , the AO loop was closed with the visible light wave front sensor on a $V \sim 14$ star $\sim 20''$ to the northeast of Sgr A* (at the time of the observations the dichroic allowing the simultaneous use of the infrared wave front sensor and the L/M bands was not available). A single imaging frame consists of 150 exposures of 0.2 s, co-added by a pipeline into a single frame with 30 s integration time. Seventy-six such images were taken. After flat-fielding, sky-subtraction, and dead/bad pixel correction, the individual frames were combined into a final SSA image of 2280 s integration time, with a Strehl ratio of $\sim 50\%$ (see also Cl  net et al. 2003). The right panel of Figure 1 shows a color composite of all three images.

In the following subsections we discuss in detail the analysis and methods we have developed and applied to carry out source counts, photometry, and astrometry in our crowded, high dynamic range AO images. Readers who wish to skip these technical details should continue with § 3.

2.1. Source Identification and Photometry

In order to facilitate the identification of sources in the extremely dense nuclear stellar cluster and to reduce the influence of the seeing halos of the numerous bright stars, we deconvolved the images prior to number counts and photometric analysis. A point-spread function (PSF) was

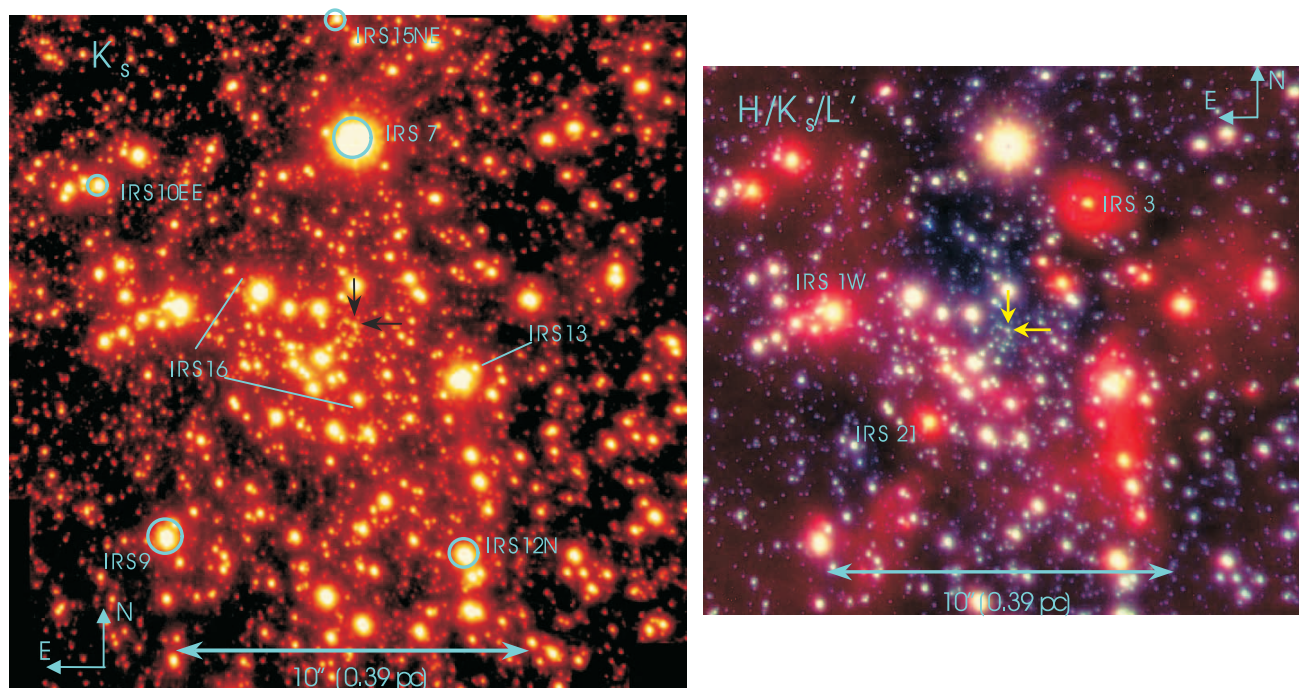


Fig. 1.—*Left:* K_s -band NAOS/CONICA SSA image of the central $\sim 20''$, taken in 2002 August (55 mas FWHM resolution; Strehl ratio $\sim 50\%$). A logarithmic color scale is used. East is to the left, and north is up. The brightest star, IRS 7 (6.7 mag), was used for infrared wave front sensing. The faintest stars visible on the image are $K_s \sim 19$. The five encircled stars (of seven in the central $30''$) are also radio SiO masers and were used for establishing the selected orientations of the infrared camera and to put the infrared data in the radio astrometric reference frame (rms $\sim \pm 10$ mas; Reid et al. 2003b). In addition, the IRS 16 and IRS 13 complexes of emission-line stars are marked. The two arrows denote the position of Sgr A*. *Right:* $H/K_s/L'$ three-color composite of the central $\sim 20''$. East is to the left, and north is up. Several bright, dusty, L -band excess stars are marked, and the two arrows denote the position of Sgr A*.

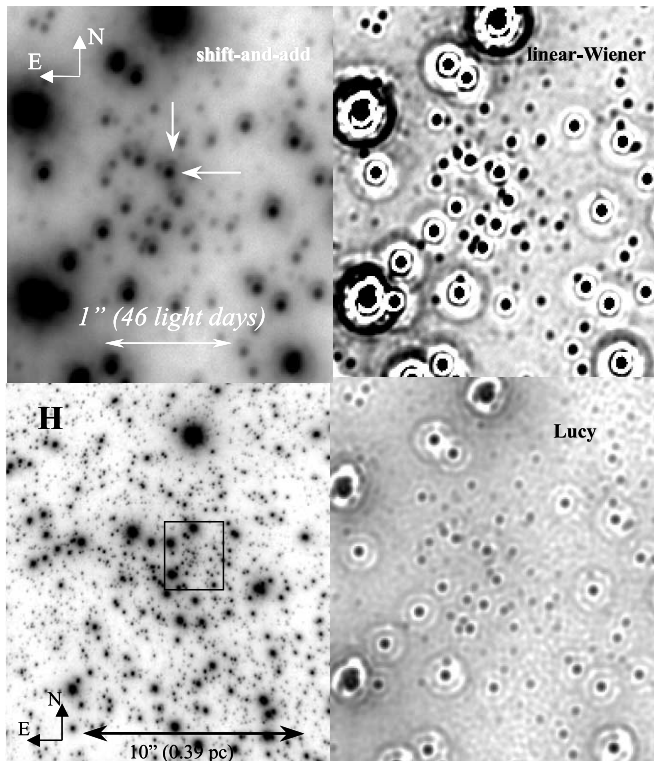


FIG. 2.—*Bottom left:* Gray-scale H -band SSA image of the central $\sim 20''$ region. A logarithmic color scale is used. The spatial scale is marked, north is up, and east is to the left. The resolution is 40 mas (FWHM), and the Strehl ratio is about 33%. *Top left:* Zoom of SSA image into the central $2''$ – $3''$ region surrounding Sgr A* (marked as a rectangle in the bottom left panel). The position of Sgr A* is marked by arrows. *Bottom and top right:* Lucy deconvolved (*bottom*) and linearly deconvolved/Wiener filtered (*top*) processed versions of the SSA image in the top left panel (same spatial scale and logarithmic color scale). In the case of the Lucy image, the final δ -function map was reconvolved with a Gaussian of 40 mas FWHM. The main purpose of the deconvolution is to remove the seeing halos, not to enhance the spatial resolution of the images. Rings in both images are artifacts of the image processing. With the exception of the vicinity of very bright and partially saturated stars, SSA, linearly, and Lucy deconvolved images show the same distribution of faint stars.

extracted from the images by taking the median of several (more than 10 in the case of the K_s - and H -band images) fairly isolated, bright, but not saturated, stars. We deconvolved the images using two methods, a linear Wiener-filter technique (Ott, Eckart, & Genzel 1999) and the Lucy-Richardson (LR; Lucy 1974) algorithm. The delta maps resulting from the LR deconvolution were reconvolved with a Gaussian PSF of the appropriate FWHM for the respective wavelengths. For comparison of the results of the different image processing techniques, Figure 2 shows the direct (SSA) image and the Wiener-filtered/linearly deconvolved and the Lucy deconvolved H -band images of the central $\sim 2''$ around the compact radio source Sgr A*. The agreement of sources identified with the different image analysis techniques is generally very good. Only within a few tenths of an arcsecond of bright (mostly saturated) stars some deterioration is caused by artifacts such as ringing. In these regions, graininess of the seeing halo, ringing, and streaks make source identification of stars 4 or more magnitudes fainter than the bright star unreliable. Figure 3 shows H -, K_s -, and L' -band Lucy deconvolved images of the central region around Sgr A*.

We identified point sources and carried out photometry with the FIND procedure from the IDL Astrolib library. The IDL FIND procedure convolves the image with a Gaussian beam prior to searching for local maxima. We found that there is no ideal choice for this parameter. Depending on the exact value of the FWHM parameter, sources may be identified or missed in densely packed regions, while various spurious sources may be detected. We therefore decided to repeat the source detection (and completeness correction; see below) procedure three times, with different values of the FWHM parameter. For construction of the final source lists we compared the lists of sources from the LR and Wiener deconvolved images, eliminating sources that showed up in only one of the lists. For the remaining stars, their photometric values were averaged, with the error taken as the deviation of the two measurements from the average. The photometric errors for the different bands are shown in Figure 4. In regions not too close to bright stars, sources of 19th magnitude are $\sim 5\sigma$ above the background in the deconvolved K_s -band image, while the H -band image is about 1.5 mag deeper. Spurious sources are detected in the seeing halos of bright stars. This problem was particularly important for the K_s band, where numerous bright stars were strongly saturated. Deconvolution techniques also tend to create faint, spurious point sources. We therefore adopted a conservative approach by applying the constraint that genuine stellar sources must be present in both the H - and K_s -band images. We verified that this procedure effectively excluded spurious detections by comparing the maps of the identified stars with the actual images.

The final lists of sources comprise between 3200 and 4000 stars, depending on the choice of the FWHM parameter, with significantly different source counts only for sources with $K_s \geq 18$. After correction for incompleteness (see below), however, the number counts at all magnitudes agree very well. For the number counts of the luminosity function and of the surface number density presented in this paper, we chose the average of the counts resulting from the different choices of the FWHM parameter. For the errors, we combined quadratically the statistical counting (Poisson) error and the maximum deviation of the counts from their average, which corresponds to a $\sim 10\%$ uncertainty at $K_s \leq 19$. We calibrated the photometry in the H , K_s , and L' bands relative to sources in the cluster. The main limitation in identifying appropriate calibration stars resulted from finding stars that were not saturated, but bright enough to be included in the Blum et al. (1996a) list. In addition, these stars should be fairly isolated because the Blum et al. (1996a) data were seeing-limited. By considering these points we tried to minimize possible systematic errors in flux calibration. For the K_s -band image, we chose four isolated stars with magnitudes between 13 and 14 from the T. Ott et al. (2003, in preparation) list (IDs 412, 284, 265, and 239). For the H -band photometry we used the Blum et al. (1996a) photometric value for IRS 33N (named IRS A11 in their list). We took IRS 33N and IRS 16CC (Blum et al. 1996a) to calibrate the L' -band data. Another point to keep in mind is that the Blum et al. (1996a) data are made for the K and L bands, while the observations presented in this paper were made with L' - and K_s -band filters. We estimate the resulting relative uncertainties of our photometry to be less than 0.1 mag at $K_s \leq 18$ ($H \leq 19$), while the absolute photometry is uncertain by 0.15 mag at H and K_s and 0.3 mag at L' .

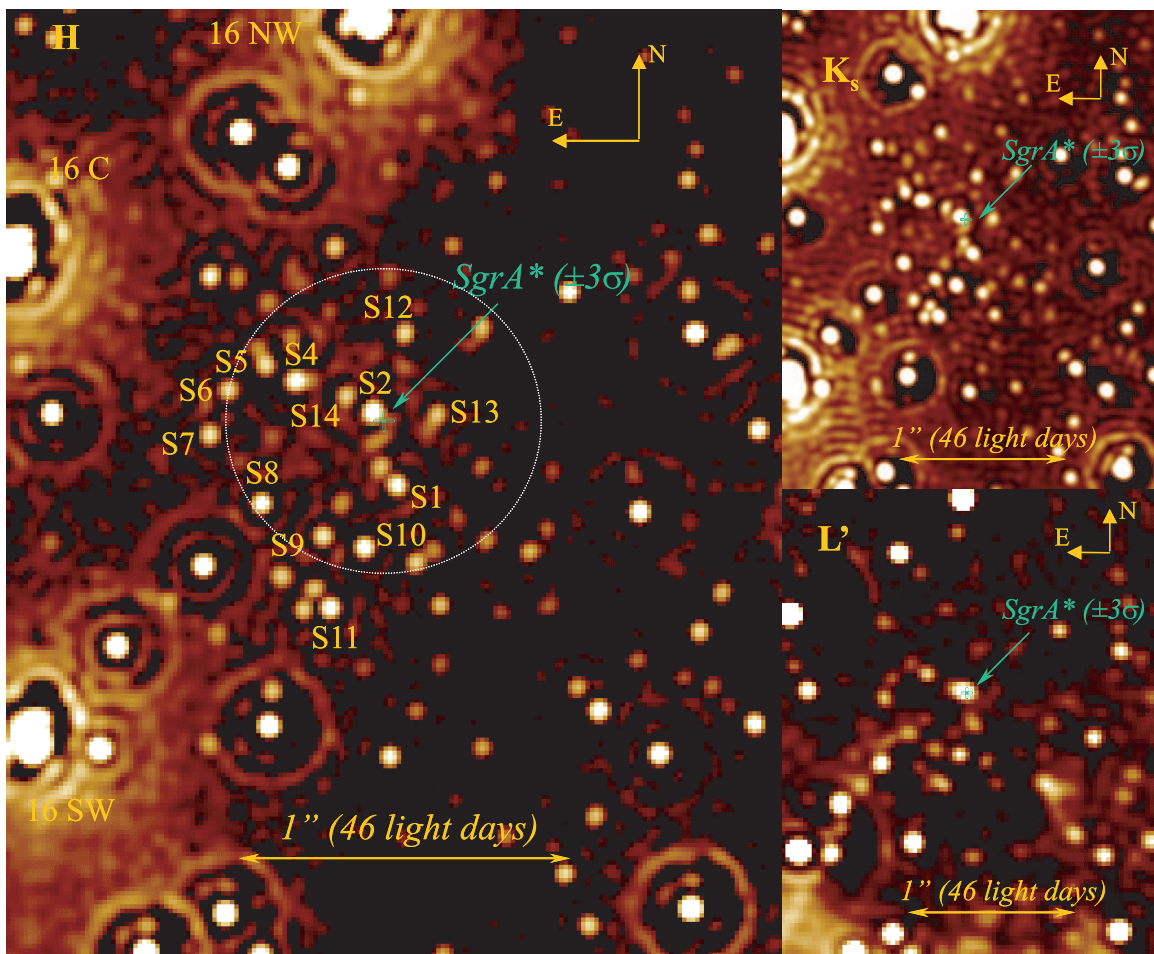


FIG. 3.—LR deconvolved images at H (left; reconvolved to 40 mas FWHM resolution), K_s (top right; reconvolved to 55 mas resolution), and L' (bottom right; reconvolved to 70 mas resolution) of the same central $2''$ region around Sgr A*. The position of Sgr A* (and its 3σ positional uncertainty) is marked by a small cross. Several of the S-sources in the Sgr A* cluster and three bright IRS 16 complex stars are marked on the H -band image. The thin dashed circle marks the radius $0''.5$, Sgr A* cluster region, containing the fastest moving stars tightly bound to the black hole (S1, S2, S12, S13, and S14). Note that for the L' -band image the visible wave front sensor was used, tracking on a star $\sim 20''$ northeast of Sgr A*. The rings around brighter stars are artifacts of the deconvolution. The faintest stars recognizable on the images are $H \sim 20$, $K_s \sim 18.5$, and $L' \sim 14$.

2.2. Incompleteness Correction

We determined the incompleteness correction for the K_s -band images with the well-known technique of first adding and then again recovering artificial stars. Taking the same PSF as used for deconvolution, we inserted artificial stars randomly into the original stellar field. The image containing the artificial stars was Wiener deconvolved, followed by source identification with the FIND procedure. We did not repeat this procedure with a LR deconvolution because of the enormous amount of computational time needed for this method. The artificial stars were spaced at intervals of $\sim 0''.5$, such that their individual PSFs did not interfere with each other. By repeating the same procedure many times with different positions for the artificial stars, we probed the image with artificial stars in a dense $\sim 0''.13 \times 0''.13$ grid. We recorded in “completeness maps” the probability of recovering a source with a given magnitude at a given position. The completeness map for stars of 18th magnitude in the K_s -band image is shown in Figure 5. Its spatial structure of course reflects the distribution of bright stars in Figure 1. Table 1 gives the overall completeness as well as the average

magnitude and standard deviation of the magnitude of the recovered artificial stars for each magnitude interval. We determined the completeness corrections for all three choices of the FIND FWHM parameter that were used to create the source lists.

TABLE 1
AVERAGE MAGNITUDES OF RECOVERED SOURCES,
SIGMAS OF AVERAGE MAGNITUDES, AND OVERALL
COMPLETENESS FOR GIVEN MAGNITUDES

K_{inp}	K_{recov}	σ	Completeness (%)
13.....	13.05	0.03	99
14.....	14.04	0.05	98
15.....	15.04	0.07	95
16.....	16.04	0.09	88
17.....	17.04	0.11	79
18.....	18.01	0.17	63
19.....	18.91	0.22	32
20.....	19.76	0.23	4

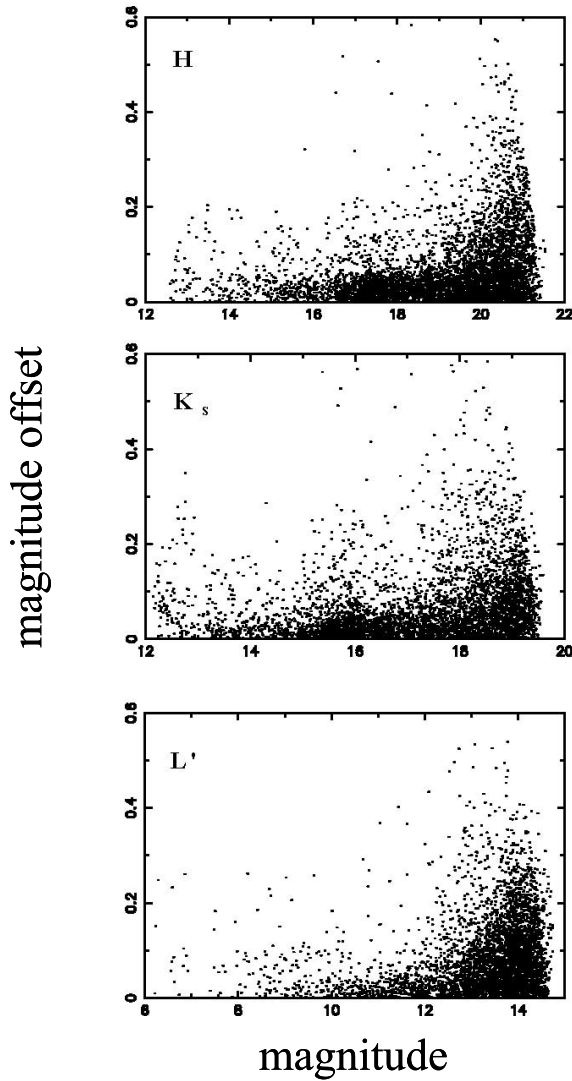


FIG. 4.—Photometric errors (in mag) as a function of magnitude as determined from a comparison of the photometry obtained on the LR and Wiener deconvolved images in H (top), K_s (middle), and L' (bottom).

2.3. Absolute Astrometry

In order to obtain astrometric positions for the stars relative to Sgr A*, we aligned the infrared images, in which the stars are observed, with the astrometrically accurate radio images, in which Sgr A* is observed (Schödel et al. 2002; Reid et al. 2003b; T. Ott et al. 2003, in preparation). For this purpose we aligned our NAOS/CONICA images with an astrometric grid using all five to seven SiO maser sources in the FOV whose positions are known through measurements with the Very Large Array (VLA) and the Very Long Baseline Array with accuracies of a few milliarcseconds (Reid et al. 2003b; circled in Fig. 1). The SiO masers originate in the central 10 AU (~ 1 mas) of the circumstellar envelopes of bright red giants and supergiants, which are also present on the infrared images. The position of the radio source Sgr A* on the infrared image, as determined by a transformation that also takes account of up to second-order terms (Reid et al. 2003b), has a 3σ uncertainty of ± 30 mas, and is denoted by arrows in the images in Figures 1 and 2 and by small crosses in Figure 3. The astrometric position of Sgr

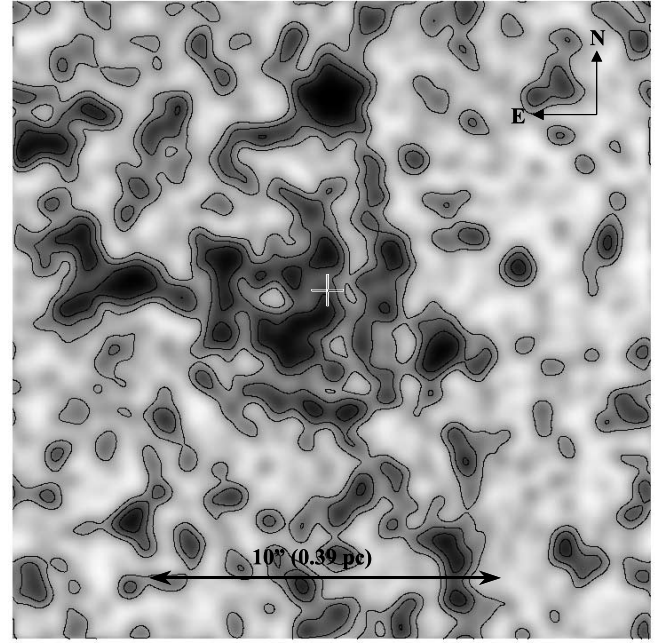


FIG. 5.—Completeness map of the K_s image at $K_s = 18$, obtained by adding artificial $K_s = 18$ stars to the image and determining the probability of recovering a star within ± 0.5 mag of the input star. The shades of gray correspond to the probability of recovering a source at a given position. Dark areas indicate the lowest probabilities. The contours outline the 20%, 40%, and 60% probability levels.

A* is coincident within a few milliarcseconds with the “gravitational force center,” as determined from the orbit of S2 (Schödel et al. 2002, 2003; Ghez et al. 2003).

2.4. Number Counts and K -Band Luminosity Function

We computed surface number densities by counting the stars in annuli with increasing radius around Sgr A*. We then corrected these number counts by dividing by the appropriate incompleteness at that radius and magnitude. In order to avoid completeness corrections significantly larger than a factor of 2 in the innermost annuli, where completeness and number counts are low for faint stars, we used only stars with K -magnitudes brighter than 17 for this analysis. In a second analysis we counted stars within $\sim 1''$ of Sgr A* by eye in the LR deconvolved H -band image. This region is devoid of bright stars, and the H -band image has the advantage of lower confusion. From the source counts, we also constructed completeness-corrected overall K -band luminosity functions (KLFs) for the circular regions within $1''.5$ and within $9''$ of Sgr A*.

2.5. Proper-Motion and Narrowband Data Sets

To study in more detail the dynamical, photometric, and spectral properties of the nuclear star cluster, we combined our NAOS/CONICA imaging and photometry with the new proper-motion and radial-velocity database of T. Ott et al. (2003, in preparation). They constructed their sample from 10 years (1992–2002) of K -band speckle imaging data at the 3.5 m ESO NTT, as well as several H/K integral field spectroscopy data sets. It contains 881 stars with proper-motion errors of less than 100 km s^{-1} , $K \leq 16$, and projected offsets from Sgr A* of up to $12''$. To separate between early- and late-type stars in the broadband maps at

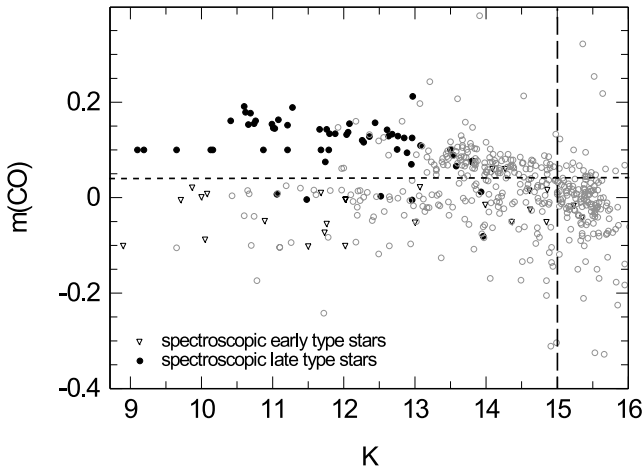


FIG. 6.—CO index [$m(\text{CO}) = m(2.29) - m(2.26)$] as a function of K -magnitude for those stars in the T. Ott et al. (2003, in preparation) proper-motion sample that also have Gemini science demonstration data set narrowband maps (open circles). Triangles denote early-type stars, and filled circles denote late-type stars confirmed by the Ott et al. spectroscopic data. For $K \leq 15$, stars with $m(\text{CO}) \geq 0.04$ are identified as late-type stars, while stars with $m(\text{CO}) < 0.04$ are identified as early-type stars.

magnitudes fainter than the current $K \sim 13$ spectroscopic limit, Ott et al. used publicly available narrowband maps taken as part of the Gemini North Galactic Center Demonstration Science Data Set. From these maps, they constructed a photometric overtone CO-band index $m(\text{CO})$ for each star in the Gemini data set, defined as

$$m(\text{CO}) = m(2.29) - m(2.26), \quad (1)$$

where $m(2.29)$ and $m(2.26)$ are the magnitudes in the narrowband filters at $2.29 \mu\text{m}$ (CO $v = 0-2$) and $2.26 \mu\text{m}$ (continuum), both calibrated on the K -band magnitude scale. Figure 6 is a plot of $m(\text{CO})$ as a function of K for those 706 stars of the Ott et al. sample with less than 100 km s^{-1} proper-motion errors that also have Gemini CO indexes. Eighty-six of these stars also have near-IR spectroscopic identifications and radial velocities (Genzel et al. 1997, 2000; Paumard et al. 2001; Gezari et al. 2002; T. Ott et al. 2003, in preparation). The spectroscopic early-type stars (H I and He I emission lines and lack of CO absorption bands) and late-type stars (CO overtone absorption bands) are marked as filled triangles and filled circles, respectively. The $m(\text{CO})$ - K plot shows that $K \leq 15$ early- and late-type stars can be separated with good confidence at $m(\text{CO}) \sim 0.04$. Fainter late-type stars have weaker CO indexes, probably because they are early-K giants. For these fainter stars it is not possible to distinguish between early- and late-type stars on the basis of the Gemini photometric index.

3. RESULTS

3.1. Multiband Imaging of the Stellar Cluster

The NAOS/CONICA science verification H and K_s images are ~ 3 mag deeper than the earlier NTT and Keck images, the H -image is the highest resolution image of the Galactic center region so far, and the L' image is the first one of the Galactic center at $\sim 0''.1$ resolution (for more details see Clénet et al. 2003). Figures 1, 2, and 3 show our basic H , K_s , and L' data sets. We have chosen a logarithmic

color scale in all three figures to emphasize the large (≥ 13 mag) dynamic range and depth ($H/K_s \leq 20$) of our H and K_s images. The faintest sources recognizable on the images are equivalent to $\sim 2 M_\odot$ A5/F0 main-sequence stars. The images in Figure 1 demonstrate the complexity of the dense stellar environment in the central parsec. Bright blue supergiants (in the IRS 16 and IRS 13 complexes), as well as red supergiants (IRS 7) and AGB stars (IRS 12N, 10EE, and 15NE), dominate the H and K_s images. At L' there is an additional group of dusty sources (IRS 1W, 3, 21). Extended L' emission comes from hot dust in the gaseous minispiral streamers comprising the most prominent features of the Sgr A* west H II region.

The immediate vicinity of Sgr A* lacks bright stars and dust. There is a concentration of $K_s \geq 14$ blue stars centered on the radio source (the “Sgr A cluster”). A number of these blue “S”-stars (Fig. 3) are now known from the proper-motion studies to in fact reside in the central 25 lt-days. The orbital parameters for six of these stars indicate that they are bound to the central object with periods between 15 and a few hundred years (Schödel et al. 2002, 2003; Ghez et al. 2003).

3.2. Spatial Distribution: Stellar Cusp

Figure 7 is a plot of the binned, stellar surface density distribution for stars as a function of projected separation from

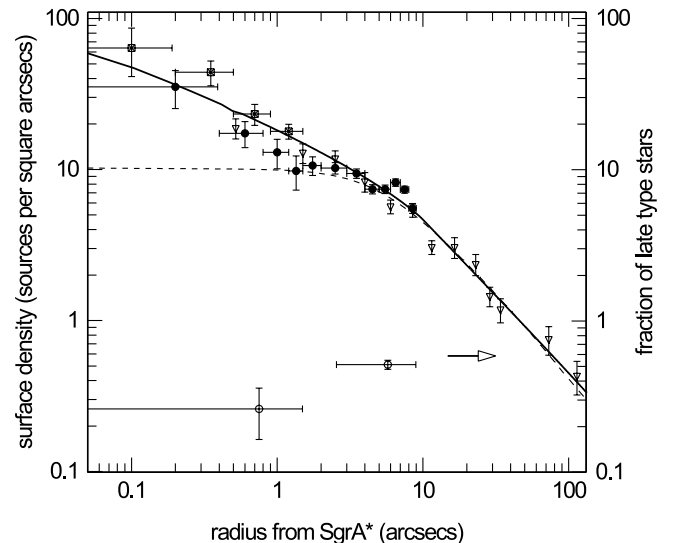


FIG. 7.—Surface density of stars as a function of projected radius from Sgr A*. Filled circles are NAOS/CONICA counts of all sources present on both H and K_s maps and with $K_s \leq 17$, corrected for incompleteness by the artificial star technique. Squares with crosses denote direct H -band NAOS/CONICA counts by eye to $H \leq 19.8$ near Sgr A*, a region devoid of bright stars. Downward-pointing triangles denote the SHARP $K \leq 15$ counts from Genzel et al. (2000), multiplied by a factor of 5.5 to best match the deep NAOS/CONICA counts in the overlap region beyond a few arcseconds from Sgr A*. The dashed curve is the model of a flattened isothermal sphere of core radius 0.34 pc fitting the counts from SHARP data. Note that at $K \sim 15$ the SHARP counts in the innermost region are only 50% complete. The continuous curve is the broken power law ($\alpha = 2$ beyond $10''$ and $\alpha = 1.4$ within $10''$) discussed in the text. Open circles at the bottom of the figure denote the fraction of late-type stars of the total $K \leq 15$ sample with proper motions and Gemini CO narrowband indexes. All vertical error bars are $\pm 1 \sigma$ and denote the total uncertainty due to Poisson statistics and, where appropriate, due to incompleteness/confusion correction ($\sim 10\%$) in each annulus. Horizontal bars denote the width of the annulus.

Sgr A*. As described in § 2.2, we have corrected the observed $K_s \leq 17$ counts from Figure 1 for incompleteness. For the higher resolution H -band data, we plot the observed $H \leq 19.8$ counts since the incompleteness correction in the central $1''.5$ is small and does not significantly vary with position. We also have determined distributions to fainter levels ($K_s \leq 18$), with very similar results. However, the incompleteness corrections at those fainter levels become large near the center and dominate the error budget. The most reliable results are obtained for the magnitude limits taken in Figure 7. For extrapolation to larger radii, we combine the NAOS/CONICA data with shallower ($K \leq 15$) but wider field NTT/SHARP number counts (Genzel et al. 2000), appropriately scaled for the best match with the deeper NAOS/CONICA data in the overlap region. As discussed in § 1, the stellar counts for projected distances $p(\text{Sgr A}^*) \geq 5''$ – $10''$ can be reasonably well fitted by a flattened isothermal sphere of core radius ~ 0.3 pc (Genzel et al. 1996 and references therein). Within a few arcseconds the new data clearly indicate an excess of faint stars above that of a flat core, already suggested by the earlier SHARP/NTT and Keck data (Eckart et al. 1995; Alexander 1999). The surface density of faint stars increases with decreasing separation from the radio source. The smoothed, two-dimensional distribution of faint stars in the H and K_s images (Fig. 8) visually confirms the existence of this “cusp” and shows that it is centered on Sgr A* [$(\Delta\text{R.A.}, \Delta\text{decl.}) = (+0''.09, -0''.15)$], within an uncertainty of $\pm 0''.2$. This is in contrast to the near-IR light distribution (Fig. 1), which is centered on the bright stars in the IRS 16 complex. Our data thus resolve the 17 year old puzzle of

why Sgr A* is offset from the $2\ \mu\text{m}$ emission peak (Allen & Sanders 1986). The offset is caused by the bright stars in the IRS 16 complex and is not a property of the majority of the faint stars in the overall nuclear cluster.

Following Alexander (1999), we have analyzed the surface number density distribution in Figure 7 with a broken power law stellar density distribution, with the simultaneous constraint that the (stellar) dynamical mass is 3.2 , 8.4 , and $27.3 \times 10^6 M_\odot$ at $R=1.9$, 3.8 , and 11 pc (subtracting from the mass distribution of Genzel et al. 1996 a $2.8 \times 10^6 M_\odot$ central point mass). The resulting fit shown in Figure 7 has the following parameters:

$$\rho_*(R) = 1.2 \times 10^6 \left(\frac{R}{10''} \right)^{-\alpha} (M_\odot \text{ pc}^{-3}), \quad (2)$$

with $\alpha = 2.0 \pm 0.1$ at $R \geq 10''$ and $\alpha = 1.4 \pm 0.1$ at $R < 10''$. We have also generalized the maximum likelihood analysis of the cusp’s slope (Alexander 1999) to take into account the incompleteness corrections. Because the radius of the extracted NAOS/CONICA field ($\sim 8''$) is smaller than the break radius of $10''$ indicated by the NTT/SHARP data, a maximum likelihood analysis of the NAOS/CONICA data alone cannot be used for a reliable determination of the parameters of the outer power law. An analysis of 856 stars in the inner $4''$, where the inner cusp dominates the total counts, indicates an inner power-law cusp with an exponent $\alpha = 1.3 \pm 0.1$, in very good agreement with our analysis of the binned data above. With these parameters, the cusp’s stellar density is $3 \times 10^7 M_\odot \text{ pc}^{-3}$ at $R = 1''$ and $7 \times 10^8 M_\odot \text{ pc}^{-3}$ at $R = 0''.1$. An alternate description of the data in Figure 7 may be a localized, Plummer model-like cusp on Sgr A* superposed on a larger scale, isothermal cluster, with a distinct break in between (N. Mouawad et al. 2003, in preparation; but see also Scoville et al. 2003). The present data cannot discriminate between these two possibilities, but the estimated stellar densities are similar. The stellar mass contained in the cusp is estimated to vary as $1.3 \times 10^4 (R/\text{arcsec})^{1.63} M_\odot$.

The analysis we just presented depends critically on the assumption that the ratio of number counts to total stellar mass (mostly in fainter not directly observed stars) does not vary with radius and environment in the Galactic center. This assumption is almost certainly violated at some level, since we argue below that giant late-type stars are destroyed and moderately massive stars are created by mergers of lower mass stars in the very dense inner region. However, we expect that these effects alter mostly the counts of the less numerous, brighter stars and not so much the fainter stars that dominate the counts. At the very least, the radial population changes make the values of the cusp density estimated above quite uncertain. Obviously, spectroscopic observations will be required for studying the properties of the fainter stars as a function of distance from Sgr A*.

Keeping this caveat in mind, the observed stellar density distribution is consistent within the uncertainties with the predictions of theoretical models for a cluster of stars surrounding a massive central black hole. These models predict the formation of a power-law cusp. The expected radial slope of the power law ranges between ~ 0.5 and ~ 2.5 , depending on the cusp’s formation scenario and on the importance of inelastic stellar collisions. Relaxed, single-mass stellar cusps have a steep slope of $\alpha \sim 7/4$ (Bahcall & Wolf 1976, 1977). Unrelaxed, initially isothermal clusters

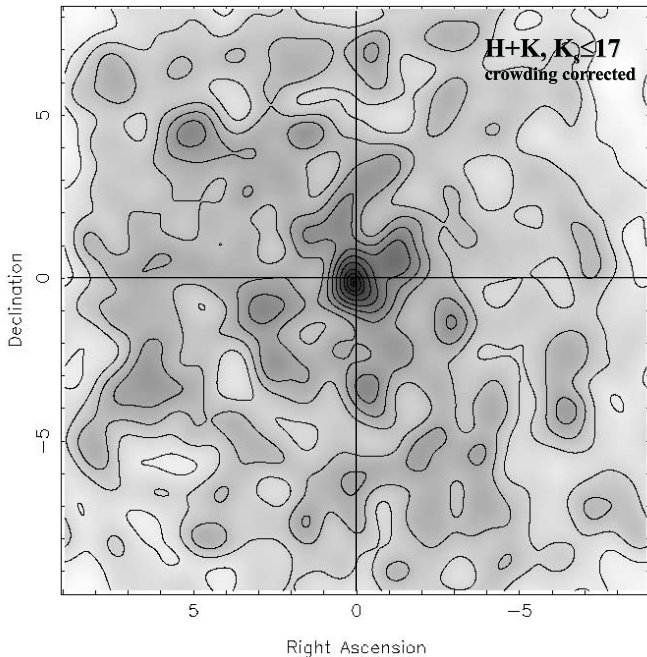


FIG. 8.—Two-dimensional map (in arcseconds relative to the map of Sgr A*) of the smoothed surface density of NAOS/CONICA sources present on both H and K_s maps corrected for crowding and incompleteness. For this purpose, the original source list maps of $H+K$ sources in each magnitude bin between K_s of 13 and 17 were smoothed with a $1''$ Gaussian and divided by the incompleteness map. The corrected maps of different magnitudes were then added. Contours are 10%, 20%, ..., 90%, 95%, 99%, and 99.9% of the peak surface density. The maximum of the stellar density is at $(\text{R.A.}, \text{decl.}) = (0''.09, -0''.15)$ relative to Sgr A*, with an uncertainty of $\pm 0''.2$.

around an adiabatically growing hole have a shallower slope of $\alpha \sim 3/2$ (Young 1980). In multimass, lower density cusps ($\rho_* < 10^7 M_\odot \text{ pc}^{-3}$), the models of Murphy, Cohn, & Durisen (1991) also predict a steep slope ($\alpha \sim 7/4$), while higher density cusps ($\rho_* \sim 10^8 M_\odot \text{ pc}^{-3}$) have flatter inner slopes due to the onset of stellar collisions ($\alpha \geq 1/2$). The models also predict that a large fraction ($\sim 80\%$) of the cusp stars near the hole should be bound to it [$\sigma^2 = v_c^2/(1 + \alpha) < v_c^2$, where $v_c^2 = GM_{\text{BH}}/R$; Alexander 1999, 2002]. Adiabatic solutions (e.g., Young 1980) that assume that the black hole grows on a timescale that is short compared to the stellar relaxation timescale do not apply to the Galactic center, which is estimated to be relaxed (e.g., Alexander 1999) and where the growth timescale of the hole is long (~ 10 Gyr).

3.3. K-Band Luminosity Function: Old Star Cluster with an Admixture of Young Stars

Figure 9 shows the KLF for the overall nuclear cluster ($p < 9''$). Figure 10 is a color-magnitude plot of the same region. Figure 11 shows the KLF of the $p \leq 1''.5$ cusp region. In both regions we have corrected the counts for incompleteness with the artificial star technique described in § 2.2, taking into account the effects of this correction on the error bars. The NAOS/CONICA data are in excellent agreement with the previous Keck and NTT data at the brighter magnitudes and extend the KLF to our completeness limit of $K_s \sim 18$. The Galactic center KLF thus samples all giants and supergiants, as well as the main sequence to spectral

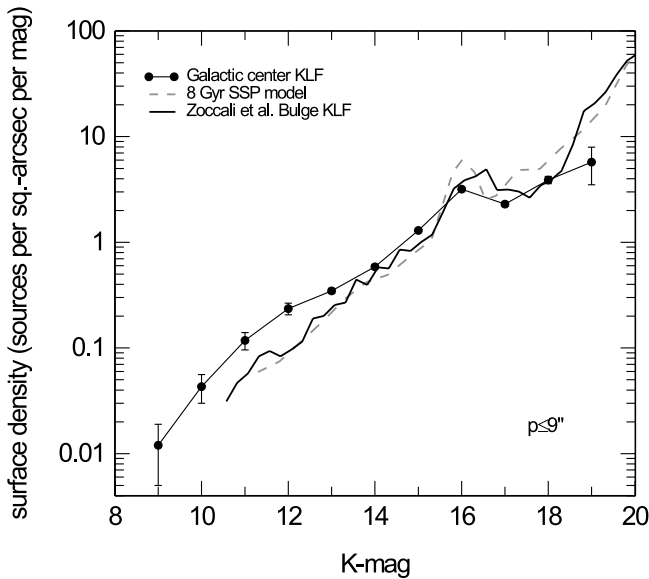


FIG. 9.—KLF (sources per square arcsecond per magnitude) as a function of K of the central $9''$ region (filled circles with 1σ error bars). The KLF points have been corrected for incompleteness as discussed in the text. Errors take into account both the Poisson error and the uncertainty of the crowding/confusion correction ($\sim 10\%$). The Galactic center data points are a combination of the new 2002 August NAOS/CONICA data (for $K_s \geq 12$) and of the SHARP/NTT data sets (T. Ott et al. 2003, in preparation), scaled in the $12 \leq K_s \leq 14.5$ overlap region for best match with the CONICA data. For comparison, the continuous curve is the KLF of the Galactic bulge on scales of degrees, and the dashed curve is a single-age (8 Gyr) stellar population model of the bulge (from Zoccali et al. 2003), both scaled vertically to match the center data and corrected horizontally to the same K -band extinction. The prominent excess hump at $K_s \sim 16$ is due to old, metal-rich, low-mass stars on the HB/RC.

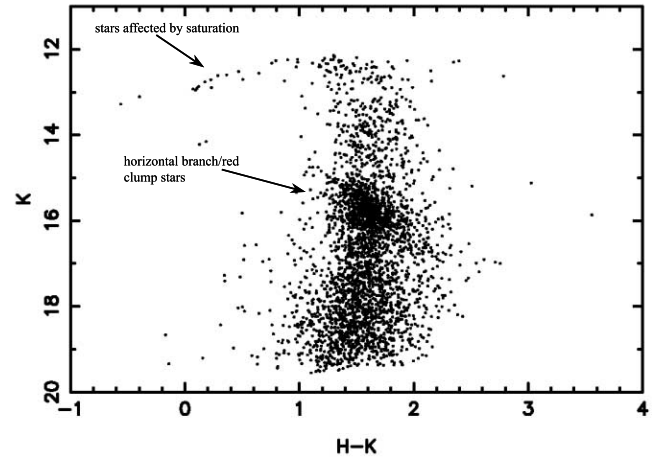


FIG. 10.—Color-magnitude diagram for the same $p \leq 9''$ region as in Fig. 9, again showing prominently the HB/RC stars. Most of the very blue stars in the color-magnitude at $K_s < 13$ are probably caused by saturation in the K_s -band image, which results in their K_s magnitudes being underestimated.

type A5/F0 ($2 M_\odot$). Since the NAOS/CONICA counts are incomplete at the brightest magnitudes because of saturation effects, we have combined the NAOS/CONICA counts and the NTT counts to a common KLF shown in Figures 9 and 11.

The overall KLF of the central $p < 9''$ (0.36 pc) region to first order is described by a power law ($d \log N/dK = \beta \sim 0.21 \pm 0.02$). In the range $14 \leq K_s \leq 19$, the overall KLF is similar to but somewhat flatter than the KLF of the bulge of the Milky Way several degrees from the center ($\beta \sim 0.3$; Alexander & Sternberg 1999; Tiede, Frogel, & Terndrup 1995; Zoccali et al. 2003) and the KLF on 30 pc scales around the center (Figer 2003). A $\beta \sim 0.3$ power law is well matched by the theoretical KLF of old stellar populations, which reflects the rate of evolution of individual stars along the red giant and asymptotic giant branches. The

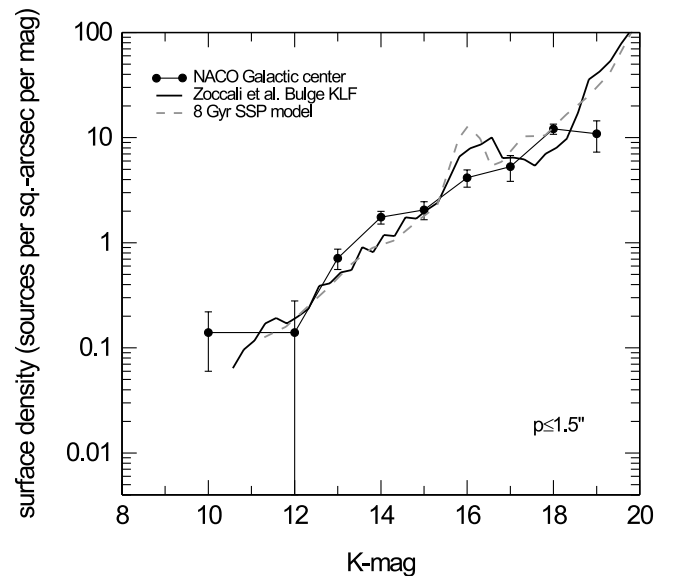


FIG. 11.—KLF (sources per square arcsecond per magnitude) as a function of K_s of the central cusp region ($\leq 1''.5$; filled circles with $\pm 1 \sigma$ error bars). Other symbols and curves are as in Fig. 9.

flatter slope of the Galactic center KLF compared to the bulge is mostly caused by an excess of the counts at $K \leq 14$, by a factor of 1.4–2. In agreement with earlier discussions (Lebofsky & Rieke 1987; Blum et al. 1996b; Davidge et al. 1997), we attribute this bright-end excess to young, early- and late-type stars. In addition, the $p < 9''$ KLF shows a prominent excess hump centered at $K_s \sim 16$, a factor of 2 above the power law. This hump is prominent in the bulge as well and on 30 pc scales around the Galactic center when all distributions are adjusted to the same (Galactic center) extinction [$A(K) = 3.2$; Rieke, Rieke, & Paul 1989; Raab 2002]. The excess can be attributed to old, metal-rich, core He-burning, horizontal-branch (HB)/red-clump (RC) stars (Tiede et al. 1995). These stars have characteristic masses of $0.5\text{--}0.8 M_\odot$. The RC stars can also readily be seen in the color-magnitude plot. The amplitude of the HB/RC excess relative to the number of giant stars making up the power-law component suggests that the Galactic bulge on average has close to solar metallicity (Tiede et al. 1995). In fact, an old (~ 10 Gyr), single-age (SSP) model with a bulge metallicity distribution deduced from the color-magnitude properties of the bulge gives a fairly good representation of the hump (Figs. 9 and 11, *dashed curves*; from Zoccali et al. 2003). We thus conclude that the hump in the KLF at $K_s \sim 16$ is most likely caused by the presence in the innermost parsec of such old, low-mass, metal-rich stars. The overall KLF of the Galactic center thus is dominated by an old cluster with an admixture of bright young stars, in excellent agreement with the spectroscopic information collected over the past decade (see § 1).

3.4. Population Changes in the Cusp

The KLF of the $p \leq 1''.5$ cusp region (Fig. 11) appears to be a featureless power law. It has a slope similar to that of the integral KLF ($\beta = d \log N / dK \sim 0.21 \pm 0.03$), but the $K_s \sim 16$ HB/RC hump appears to be absent. Compared to the $p \leq 9''$ and bulge KLFs, this deficit is significant at the 4–5 σ level. Relative to the $p \leq 9''$ KLF, there may also be an excess of stars at $13 \leq K_s \leq 15$ (Fig. 11). We conclude that the cusp probably lacks old, low-mass, HB/RC stars. The cusp probably also lacks late-type giants. The fraction of $K \leq 15$ late-type stars, as determined from the narrowband Gemini indicator, drops from 50% at $p \geq 5''$ to 25% at $p \leq 1''.5$ (Fig. 7). Considering again the effect of the foreground and background cluster stars, the intrinsic late-type fraction in the cusp region proper must be even lower. Assuming a simple two-component model with a late-type fraction of 50% in the outer region, the cusp's content of $K \leq 15$ late-type stars must intrinsically be $\leq 15\%$. However, because of the small numbers of late-type stars in the very center (seven within $1''.5$), the statistical significance of this difference

naturally is only 3 σ . We conclude that the content and/or the properties of the stars in the cusp are different from those in the outer regions. The dense cusp may lack old, low-mass stars. Alternatively, and more likely, in the dense environment low-mass stars ascending the red giant branch are stripped of their entire envelopes by physical collisions or close tidal encounters (see below and Appendix A). Losing their envelopes well before their helium cores reach critical mass for helium ignitions, these stars would evolve directly to become helium white dwarfs, skipping the HB/RC phase. This could account for the absence of the HB/RC hump in the KLF and the lower fraction of red giants.

Taking the KLF of the cusp, we can estimate the number of stars as a function of K that are expected to reside within different radii from Sgr A*. We list these numbers in Table 2 for different magnitude (or mass) limits, for $R = 1'', 0''.1$, and $0''.03$, and for two values of β . The value of $\beta = 0.21$ is the slope determined from the observed KLF for $K_s \leq 18$. A value of $\beta = 0.35$ fits the bulge KLF (Alexander & Sternberg 1999) or a model of an old star cluster (Zoccali et al. 2003; Fig. 11). To normalize to the observations, we use the value of 56 stars within $p \leq 1''$ and $K_s \leq 17$, as determined from the broken power law fit in Figure 7.

The $R = 0''.03$ numbers are interesting since they give an impression of the number of stars with orbital periods ≤ 2 yr and orbital velocities ≥ 3000 km s $^{-1}$ that may be accessible to future interferometric observations of the Sgr A* cusp. For the likely range of the faint-end KLF slope and for a realistic observational limit of $K_s \leq 20$, Table 2 suggests that one ought to expect one or several such stars to be present at any given time if they move on circular orbits. The present data suggest a large fraction of highly eccentric orbits (Schödel et al. 2003). In that case the number of fast-moving stars would be significantly larger. In fact, two such stars (S2 and S14) have already been observed (Schödel et al. 2002, 2003; Ghez et al. 2003). The prospects thus are good for using interferometry to sample stars closer to the central black hole than presently possible with AO on 10 m class telescopes.

The total number of unobserved, low-mass stars ($0.5\text{--}1 M_\odot$) extrapolated with the KLF slope, in combination with the mass model of § 3.2 above, can also be used to compute the average stellar mass in the cusp. For $\beta = 0.21$ this average mass is $33 M_\odot$ to a limiting magnitude of $K_s = 21$ (corresponding to $1 M_\odot$ main-sequence stars) and $13 M_\odot$ to $K_s = 23$ (corresponding to $0.5 M_\odot$ main-sequence stars). For $\beta = 0.35$ the average masses to the same K_s limits are 8.9 and $1.8 M_\odot$. Assuming a Salpeter mass function (for lack of a better choice) with power-law slope in density $\gamma = 2.35$ and with lower mass limits of $m_{\min} = 0.5$ and $1 M_\odot$, the average stellar masses are 1.6 and $3.1 M_\odot$, respectively. For

TABLE 2
NUMBERS OF STARS EXPECTED FROM OUR MASS/KLF MODELING FOR DIFFERENT MAGNITUDE/MASS LIMITS,
TWO VALUES OF THE KLF FAINT-END SLOPE β , AND THREE DIFFERENT OUTER RADII FROM SGR A*

MAGNITUDE LIMIT	$\beta = 0.21$			$\beta = 0.35$		
	$p \leq 1''$	$p \leq 0''.1$	$p \leq 0''.03$	$p \leq 1''$	$p \leq 0''.1$	$p \leq 0''.03$
$K_s \leq 18.5$: A0 V/ $3.5 M_\odot$	114	3	0.4	189	4	0.6
$K_s \leq 19.5$: A5 V/ $2.2 M_\odot$	185	4	0.7	423	10	1.4
$K_s \leq 21$: G1/2 V/ $1.0 M_\odot$	383	9	1.3	1416	33	5
$K_s \leq 23$: M0 V/ $0.5 M_\odot$	1000	24	3.4	7100	166	23

a shallower initial mass function of $\gamma = 1.5$, the corresponding average stellar masses are $7 M_{\odot}$ ($m_{\min} = 0.5 M_{\odot}$) and $10 M_{\odot}$ ($m_{\min} = 1 M_{\odot}$). KLF slope, number counts, and mass model thus are consistent with each other in either one of two regimes. If the cusp has a Salpeter IMF, then the faint-end KLF must have a slope significantly steeper than $\beta = 0.21$ and extend to $0.5 M_{\odot}$ or lower masses. Alternatively, if the faint-end KLF slope remains near the value of $\beta = 0.21$ characteristic of the $K_s \leq 18$ data, then the IMF must be significantly shallower than a Salpeter IMF, thus containing more high-mass stars. The latter explanation would be favored if indeed stellar mergers are effective, as argued in § 4.4. The difference in number counts at $K_s \sim 19$ between a $\beta = 0.35$ and a $\beta = 0.21$ KLF is about a factor of 2. Ultradeep *H*-band NAOS/CONICA observations may be able to test whether such a steepening of the faint-end KLF does occur.

3.5. Young, Massive Stars in the Central Star Cluster

There are several pieces of evidence that the cusp contains many young, massive stars. Moderate-resolution infrared spectroscopy is available for many bright stars with $K \leq 13$ and $p \geq 1''$ (Genzel et al. 1996, 2000; Paumard et al. 2001; T. Ott et al. 2003, in preparation). The data, as summarized in Ott et al. show that five of seven stars at $p \leq 3''$ with $K \leq 11.5$, and six of 11 with $K \leq 12$, are early-type, hot, emission-line stars (He I stars). The $K_s \leq 13$ early-type stars at $p \geq 1''$ must be young. Their near-IR spectral properties indicate that they are blue supergiants (Of), luminous blue variables (LBVs), or late-type, Wolf-Rayet (WN/C) stars with ages of 2–7 Myr and masses of 30 to $120 M_{\odot}$ (Krabbe et al. 1995; Tamblyn et al. 1996; Najarro et al. 1997; Ott et al. 1999; Paumard et al. 2001; Figer et al. 1998, 1999; Cotera et al. 1999; Figer 2003). There is a prominent concentration of these stars in the IRS 16 and IRS 13 complexes. Ott et al. (1999) found that the bright He I emission-line star IRS 16SW is an eclipsing binary of mass $\sim 100 M_{\odot}$. The alternative possibility that the hot emission-line stars are rejuvenated products of mergers from lower mass, old stars can be excluded for stars outside the central few tenths of an arcsecond (see Appendix A). The stellar density several arcseconds or more away from Sgr A* is definitely too low to account for mergers to produce stars more massive than $10\text{--}20 M_{\odot}$ (Genzel et al. 1994; Lee 1994). Furthermore, the properties of the bright emission-line stars are essentially identical to the massive stars in the Quintuplet and Arches clusters, 30–50 pc away from Sgr A*, in much lower density environments (Figer et al. 1998, 1999; Cotera et al. 1999; Figer 2003).

Within the Sgr A* cluster ($p \leq 0''.5$) Gezari et al. (2002) and Ghez et al. (2003) have recently reported AO-assisted spectroscopy of several stars with the Keck telescope. S2 exhibits H I Br γ absorption and clearly is a hot star with an equivalent main-sequence identification of O8/B0. S1 and the fainter star S0-16 do not exhibit CO absorption features and thus are very likely early-type stars, with equivalent main-sequence identifications of B0 (S1) and B5 (S0-16) (Genzel et al. 1997; Eckart, Ott, & Genzel 1999; Figer et al. 2000; Gezari et al. 2002). Based on narrowband, speckle spectrophotometry, Genzel et al. (1997) concluded that S8 and S11 are early-type stars as well. The S-stars near Sgr A* represent the possible $K_s \sim 14$ excess found in the KLF.

3.6. Two Kinematic Components of Young Stars

We next use the narrowband colors and proper motions of the T. Ott et al. (2003, in preparation) sample to demonstrate that the somewhat fainter ($K_s \leq 15$) spectrophotometrically identified early-type stars in the central few arcseconds must also be young and can be separated into two separate kinematic components. Consider the normalized angular momentum along the line of sight, $J_z/J_z(\max)$, which we define as

$$J_z/J_z(\max) = (xv_y - yv_x)/pv_p, \quad (3)$$

where v_x , v_y , and v_p are the right ascension, declination, and total proper motion velocities of a star at (x, y) on the sky at projected radius p . The term $J_z/J_z(\max)$ is ~ -1 , ~ 0 , and $\sim +1$, depending on whether the stellar orbit projected on the sky is mainly counterclockwise tangential, radial, or clockwise tangential with respect to the projected radius vector from the star to Sgr A*. Note that stars moving tangentially in projection also must move tangentially in three dimensions. Stars moving radially in projection, however, may move radially in three dimensions, tangentially, or a mixture of the two, depending on their location along the line of sight. Figure 12 shows the distribution of $J_z/J_z(\max)$ as a function of p for late- and early-type stars, as identified from the narrowband CO index (Fig. 6). Figure 13 is a plot of the spatial distribution on the sky of early- and late-type stars with clockwise, counterclockwise, and radial orbits. For convenience, we divided here the normalized angular momentum range into three bins: clockwise tangential

$$[J_z/J_z(\max) \geq 0.6],$$

counterclockwise tangential

$$[J_z/J_z(\max) \leq -0.6],$$

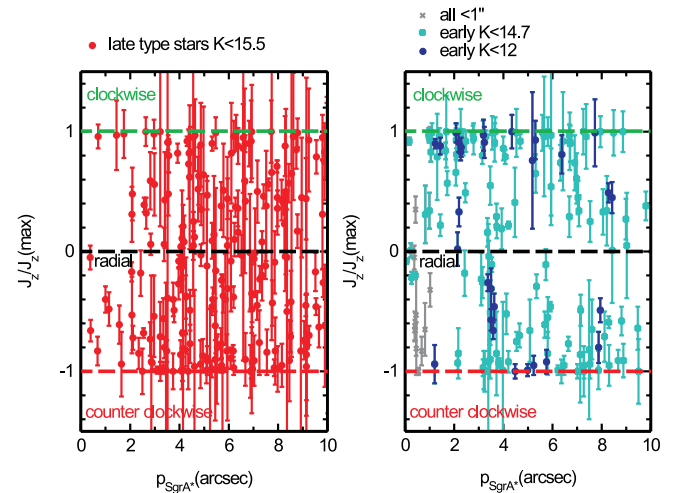


FIG. 12.—*Left*: Normalized angular momentum along the line of sight [$J_z/J_z(\max)$] as a function of projected separation from Sgr A* for the $K \leq 15.5$ late-type stars [filled circles: $m(\text{CO}) \geq 0.04$]. *Right*: Same, for the early-type stars [$m(\text{CO}) < 0.04$], with $K \leq 14.7$ (squares with crosses) and $K \leq 12$ (filled circles), all from the T. Ott et al. (2003, in preparation) sample. In addition, crosses denote the other $p \leq 1''$ stars in the Ott et al. sample whose spectral properties are not known. In this plot, clockwise projected tangential orbits are at $J_z/J_z(\max) = +1$, counterclockwise projected tangential orbits are at $J_z/J_z(\max) = -1$, and radial orbits are at $J_z/J_z(\max) = 0$. All error bars are $\pm 1 \sigma$.

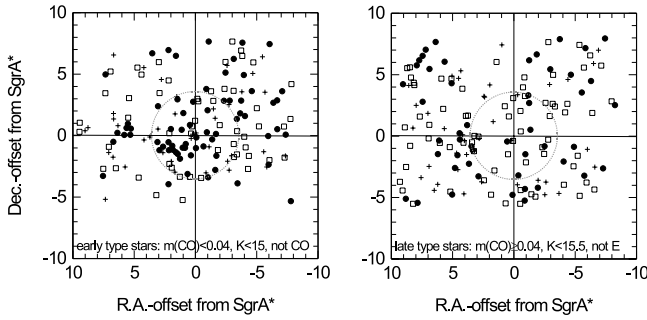


FIG. 13.—Spatial distribution of different projected orbits for early-type stars (*left*) and late-type stars (*right*) in the T. Ott et al. (2003, in preparation) sample [for $K \leq 15$, cutting at $m(\text{CO}) = 0.04$, as in Fig. 8]. Filled circles denote projected clockwise tangential orbits [$J_z/J_z(\text{max}) \geq 0.6$], open squares denote projected counterclockwise tangential orbits [$J_z/J_z(\text{max}) \leq -0.6$], and plus symbols denote projected radial orbits [$-0.3 \leq J_z/J_z(\text{max}) \leq 0.3$]. The dotted thin circles marks the cusp region with a radius of $3''$ around Sgr A*, which also contains most of the bright emission-line stars in the IRS 16 complex (Fig. 1).

and radial

$$[-0.3 \leq J_z/J_z(\text{max}) \leq 0.3].$$

The isotropic late-type stars serve as our comparison sample. They exhibit a random distribution of line-of-sight angular momenta (Fig. 12, *left*; Fig. 13, *right*); $21\% \pm 9\%$ and $36\% \pm 11\%$ of the late-type stars within $3''$ and $22\% \pm 3\%$ and $31\% \pm 4\%$ within $10''$ are on clockwise and counterclockwise orbits, respectively. In contrast, the early-type stars show a preponderance of tangential and a lack of radial orbits (Fig. 12, *right*). Within the central $3''$, $51\% \pm 10\%$ and $18\% \pm 6\%$ of the early-type stars are on clockwise and counterclockwise tangential orbits, respectively. Between $3''$ and $10''$ there are about equal numbers of clockwise and counterclockwise tangential motions but still a lack of radial orbits. The preponderance of clockwise tangential velocities near Sgr A* is also graphically apparent in the overdensity of filled circles within $3''$ from Sgr A* in the left panel of Figure 13. In marked contrast to the random pattern of the late-type stars broken up into the same three groups (Fig. 13, *right*), early-type stars with clockwise tangential orbits dominate within a few arcseconds of Sgr A* and bunch up in the IRS 16 complex east-southeast of Sgr A*. This means that most of the early-type stars in the central $10''$ are not relaxed and belong to one of two kinematic components with opposite line-of-sight angular momenta.

The line-of-sight velocities also confirm that the late-type stars are relaxed but early-type stars are not. Apart from an average blueshift in the central $10''$, the late-type stars show a random distribution of line-of-sight velocities (McGinn et al. 1989; Sellgren et al. 1990; Genzel et al. 1996; Haller et al. 1996). In contrast, early-type stars north of Sgr A* are almost all blueshifted, while stars south of Sgr A* are almost all redshifted (Genzel et al. 1996, 2000; Paumard et al. 2001). This clear-cut pattern is shown in the right panel of Figure 14 and is indicative of coherent rotation, with a direction opposite (counter) to that of the overall Galactic rotation.

3.7. Two Coeval, Rotating Disks of Young Stars

This global rotation pattern has previously been discussed by Genzel et al. (1996, 2000) and Paumard et al.

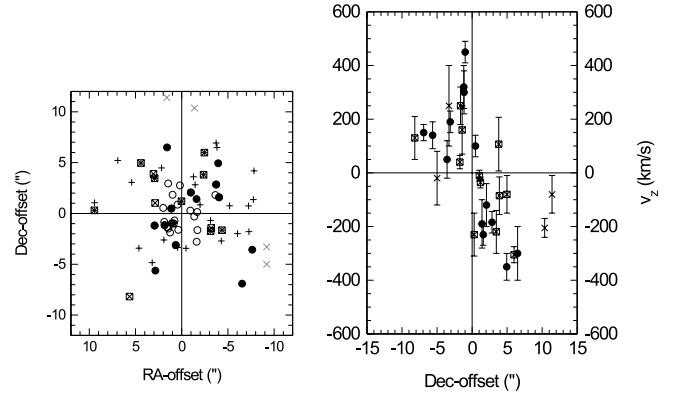


FIG. 14.—*Left*: Spatial distribution of early-type stars. Clockwise, spectroscopically identified stars (three velocities) are marked by filled circles, $K_s \leq 14$ clockwise proper motion stars (two velocities) are marked by open circles, counterclockwise spectroscopic stars are marked by squares with crosses, $K_s \leq 14$ counterclockwise proper motion stars are marked by plus symbols, and spectroscopic stars without proper motions are marked by crosses. *Right*: Line-of-sight velocity as a function of declination offset from Sgr A*, for the different types of early-type stars. Symbols are as in the left panel.

(2001). Genzel et al. (2000) found that the three-dimensional velocity field could be matched by a rotating disk at inclination $\sim 140^\circ$ (or 40° , depending on the definition of the angles) but noted that the fit was poor and that “a better description ... probably is a dynamically hot and geometrically thick rotating torus ...”. In the following we use the new data set of T. Ott et al. (2003, in preparation) for a better determination of the disk parameters and for an investigation of whether the two kinematic components of early-type stars discussed in the last section can both be fitted by rotating disks. For this purpose, we followed Levin & Boloborodov (2003) and first analyzed all 14 clockwise [$J_z/J_z(\text{max}) \geq 0$] early-type stars with three velocities, as well as all 12 counterclockwise [$J_z/J_z(\text{max}) \leq 0$] early-type stars with all three velocities measured. We explored whether there exists a disk of inclination i and projected major-axis position angle (line of nodes) on the sky ϕ_0 that fits the velocity field of all stars. We searched for a vector $\mathbf{P}(i, \phi_0)$ (perpendicular to the disk) for which the observed velocities of the stars along \mathbf{P} are minimized. For the 14 clockwise stars we find that the best-fitting plane ($i = -120^\circ \pm 7^\circ$ and $\phi_0 = -60^\circ \pm 15^\circ$) fits the data with $\chi^2_{\text{red}} \sim 4$ (Fig. 15, *left*). Most of the deviation from a common plane is caused by one star located $9''$ southwest of Sgr A* (AFNW). Our proper motions at such large distances strongly depend on the assumed values for the second-order distortion terms in our astrometric solution. Since these terms are not as well constrained by the SiO maser stars in the field as the first-order terms, there may be large systematic uncertainties for proper motions this far from the center. Taking only stars with separations $7''$ or smaller from Sgr A* (Fig. 15, *left*, filled circles) reduces the number of stars to 12 and χ^2_{red} to 2. The clockwise early-type stars with three velocities thus can be described very well by a thin rotating disk (at an average distance of $2''$ – $4''$ from the center). The derived disk orientation agrees with that obtained by Levin & Boloborodov (2003), who used the earlier Genzel et al. (2000) proper-motion/radial-velocity set. A position angle of -40° to -60° is also consistent with the spatial elongation of the stars in the x - y plane (Fig. 14, *left*;

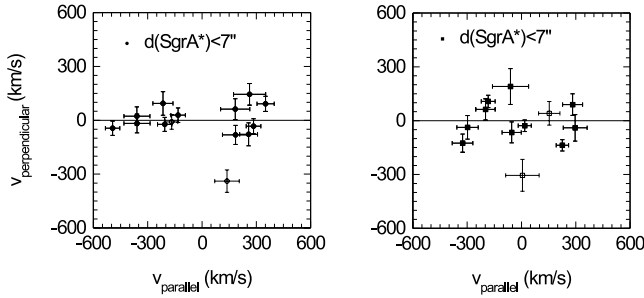


FIG. 15.—Velocity parallel to the best disk plane (horizontal) and perpendicular to the disk plane (vertical) for all early-type stars with three velocities. The left panel shows stars that move clockwise; the right panel shows stars that move counterclockwise. The velocity data are from T. Ott et al. (2003, in preparation). Open symbols mark stars outside the central $7''$, where proper motions are less reliable. For the clockwise stars, motions are plotted with respect to the best-fitting disk plane with an inclination of 120° (angle relative to the plane of the sky) and with a position angle on the sky of -60° (angle on the sky, increasing east from north). For this disk plane, the reduced χ^2 is 3.9 if all 14 stars are included and 1.9 if stars with $p \geq 7''$ are eliminated. For the counterclockwise stars, the best-fitting plane (reduced $\chi^2 = 5.1$, and 4.8 after elimination of $p \geq 7''$ stars) has an inclination of -40° and a position angle of 160° .

with the exception of AF and AFNW $9''$ – $10''$ southwest). For the 12 counterclockwise stars, the best-fitting plane ($i = -40^\circ \pm 15^\circ$ and $\phi_0 = 160^\circ \pm 15^\circ$) fits the data to $\chi^2_{\text{red}} = 5$ (Fig. 15, *right*). Removing the two stars more than $7''$ away from Sgr A* (*open squares*) reduces χ^2_{red} somewhat to 4.8. Again, a low-inclination disk is consistent with the spatial distribution of the counterclockwise stars in Figure 14 (*left*). A rotating thin disk model thus also fits the counterclockwise stars, but the deviations from the model are somewhat larger than for the clockwise stars. The characteristic radius of the counterclockwise stars is $4''$ – $7''$.

In the next step we explored whether also the many other clockwise and counterclockwise stars with proper motions (but without 3-velocity components) can be fitted by the same disk parameters. From coordinates and proper motions one can construct two angles, $\alpha(x, y)$ and $\beta(v_x, v_y)$ ($\tan \alpha = x/y$, $\tan \beta = v_x/v_y$), which are independent of the radius in the disk but are functions of i and ϕ_0 . The thick curve in Figure 16 denotes the loci of stars in a disk with parameters derived above for the clockwise stars, while the other curves denote model disks with parameters within the uncertainties of the best fit. The filled and open circles denote the clockwise tangential stars [$J_z/J_z(\text{max}) \geq 0.6$] for $p \leq 5''$ and $K \leq 14$ and 15, respectively. Clearly, these fainter stars fit the input disk model (of the 14 stars with 3-velocities) very well. Likewise, the counterclockwise tangential stars fit the input disk model of the 12 stars with 3-velocities. In contrast, late-type stars selected in the same manner [$J_z/J_z(\text{max}) \geq 0.6$, $K \leq 14, 15$] do not fit a rotating thin disk model. They exhibit a large scatter around the best-fit disk model (Fig. 16, *right*). A similar check can also be done with the counterclockwise stars. However, because of the small inclination, the data are not as well constrained as in the clockwise subset.

We conclude that the dynamics of most early-type stars can be well fitted by two rotating and geometrically fairly thin disks. Levin & Boloborodov (2003) conclude from their analysis that the (clockwise) disk may be geometrically infinitely thin. Our own analysis suggests that a finite thickness or moderate warping of the disks is probably still con-

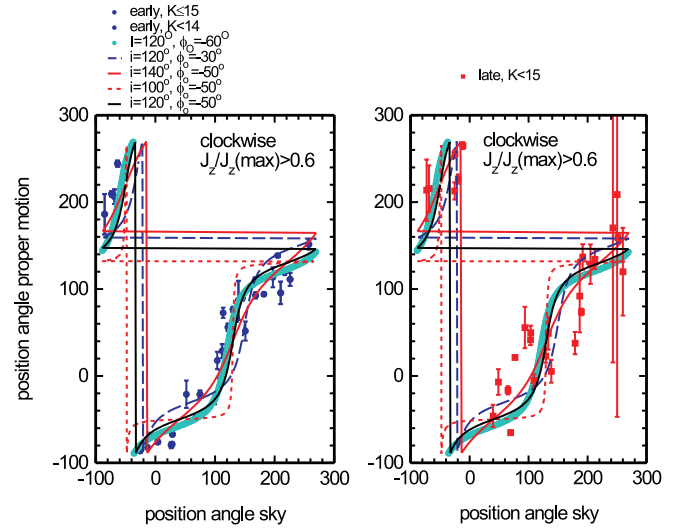


FIG. 16.—*Left*: Position angle on the sky [$\tan(x/y)$; *horizontal*] and position angle in proper-motion velocity [$\tan(v(x)/v(y))$; *vertical*] for clockwise tangential proper motion stars (filled circles: $K_s \leq 14$; open circles: $K_s \leq 15$). The different curves (marked on the figure) denote models of different inclination and position angle close to the best-fitting model in Fig. 15. *Right*: Same, but for clockwise tangential late-type stars.

sistent with the data, especially for the counterclockwise stars. Figure 17 summarizes the orientation of the two derived disks. The two disks are at large angles relative to each other and effectively counterrotate but do share a common projection of their rotation vectors that are opposite to that of Galactic rotation (Fig. 14, *right*). The clockwise disk is more compact, with a characteristic radius of $2''$ – $4''$, while the counterclockwise disk has a characteristic radius of $4''$ – $7''$.

The stellar content of the two disks is essentially identical. Of the 14 clockwise stars with spectroscopic identifications in T. Ott et al. (2003, in preparation), there are four Of/LBV, five WNL (7–9), one WNE (5/6), and four WCL (8/9) stars. Of the 12 spectroscopic counterclockwise stars, there are two Of/LBV, three WNL, six WCL, and one WCE (5/6). The agreement of the different subtypes of blue

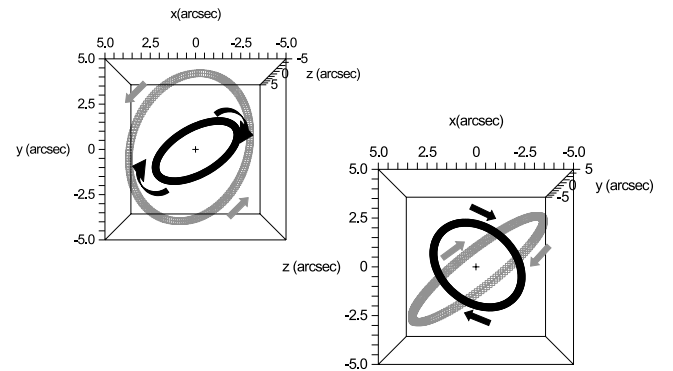


FIG. 17.—Three-dimensional projections of the two best-fit, rotating disks and their rotation directions. The inner thick curve denotes the characteristic radius of the more compact, clockwise stars, while the outer, light-shaded curve denotes the counterclockwise stars; x and y are the coordinates on the sky (east-west and north-south), with eastward counting positive in x ; z is the line-of-sight coordinate, with the observer being located at large negative z . In the lower right panel, the top parts of both the inner and the outer disks move toward the observer (counter to Galactic rotation).

supergiants and Wolf-Rayet stars is remarkable. The lifetimes of these different subtypes is no more than a few hundred thousand years, and the WC phase occurs just before explosion as a supernova (Maeder & Meynet 1994). Hence, the two disks must have formed at the same time, within less than 1 Myr.

The early-type (S-) stars in the Sgr A* cluster ($p \leq 0''.5$) show a different angular momentum distribution (Fig. 12, *right*). Keeping in mind that a few of these stars may only be projected to lie in the central arcsecond, the Sgr A* cluster stars do not show an excess of tangential orbits. On the contrary, a more detailed analysis shows an excess of radial orbits (Genzel et al. 2000; Schödel et al. 2003). Fifty-four percent ($\pm 14\%$) of the 35 observed stars in the Sgr A* cluster are on radial orbits. These stars are probably observed near the apoapse of their orbit (roughly twice the semimajor axis), where they spend most of their time. It is therefore likely that the radial stars are tightly bound to the black hole, with semimajor axes of order 20 mpc. This statistical inference, together with the direct derivation of semimajor axes of less than 10 mpc for the six stars in the inner cusp whose orbits were solved (Schödel et al. 2003), suggests that the Sgr A* cluster as a whole is tightly bound to the black hole. The orbital planes of those stars, as far as they are constrained by the current data, are significantly different from the two disk planes of the early-type stars at $p \geq 1''$. For instance, S2 has a clockwise angular momentum, but its orbital plane is 70° off the plane of the clockwise early-type stars discussed above. Levin & Beloborodov (2003) have commented that such large offsets may be explained by relativistic Lense-Thirring precession of a star originally in the same plane as the stars farther out.

In summary, we find compelling evidence from different arguments—KLF, spectra/narrowband photometry, dynamics—that the stellar cusp centered on the massive black hole candidate Sgr A* does not primarily consist of old, low-mass stars with properties similar to those found in the Galactic bulge. Late-type giants and HB/RC stars seem to be less frequent. The cusp contains a surprising number of unrelaxed and apparently young, massive stars, including the very short lived He I emission-line stars with masses 30–100 M_\odot that reside in two rotating disks. This result is not consistent with theoretical expectations for a steady state cusp, which predict that such a cusp should be dynamically relaxed (Bahcall & Wolf 1976, 1977; Murphy et al. 1991).

The properties of the nuclear region are not consistent with static equilibrium. Episodic star formation and stellar transformations are required.

3.8. Mid-IR Excess of S2: Probing the Accretion Flow onto Sgr A*?

Table 3 lists the $H/K_s/L'$ photometry of S2/Sgr A* and 11 other stars in the central Sgr A* cluster as derived from the new NAOS/CONICA photometry. At H and K_s the peak emission of S2/Sgr A* is definitely centered on S2 (and off Sgr A*), and we can only deduce upper limits to the magnitudes of Sgr A* (Fig. 3; Table 2). The $H-K_s$ color of S2 (1.3 ± 0.1 mag) compares well to the average value of the 11 other $H < 17$ stars within $0''.7$ of Sgr A* ($\langle H-K_s \rangle = 1.42 \pm 0.03$). This color is consistent with that of blue stars [$(H-K_s)_0 = -0.04$] behind the standard Galactic center K -band extinction of ~ 3 mag (Rieke et al. 1989) and thus is consistent with their being early-type stars, as discussed above. However, the K_s-L' color of S2+Sgr A* (2.9 ± 0.1 mag) is 0.65 mag redder than the same 11 stars ($\langle K_s-L' \rangle = 2.25 \pm 0.15$). S2+Sgr A* thus has a significant L' excess relative to stars with the same $H-K$ colors (see also Clénet et al. 2003). Extrapolating from the average color of the nearby stars, the excess flux density corresponds to 4.9 mJy. Correcting for a K -band extinction of 3.2 mag, or an L' extinction of 2.1 mag [Raab 2002; $A(H) = 5.1$, $A(K_s) = 3.2$, and $A(L') = 2.1$], the dereddened L' -band excess flux density of S2+Sgr A* is about 33 mJy. Gezari et al. (2002) and Ghez et al. (2003) find that the K -band flux density and spectrum of S2 is consistent with a O8/O9 main-sequence star, which would have a mass of 15–20 M_\odot , a bolometric luminosity of $10^5 L_\odot$, and a temperature of 35,000 K. Such a main-sequence star would not be expected to have a very dense, dusty wind that could account for the observed L' emission. What then causes the L' excess of S2?

One obvious possibility is that the excess is due to emission from Sgr A* itself, in which case we have the first detection of the mid-infrared emission from the accretion region in the immediate vicinity of the black hole. This explanation may be supported by the spatial distribution of the L' emission. The peak of the L' emission is closer to Sgr A*, and the L' emission of S2/Sgr A* appears to be spatially extended (Fig. 3, *bottom right*). The FWHM of S2+Sgr A* on the L' Lucy map (Fig. 3) is $95 \text{ mas} \times 70 \text{ mas}$ (east-west \times north-south), compared to $70 \text{ mas} \times 70 \text{ mas}$ for unresolved stars.

TABLE 3
 $H/K_s/L'$ MAGNITUDES IN 2002 AUGUST OF $H < 17$ SOURCES AND SGR A* IN THE CENTRAL $0''.7$

Source	$x(\text{Sgr A}^*)$	$y(\text{Sgr A}^*)$	H	δH	K_s	δK_s	L	δL	$H-K_s$	K_s-L'
Sgr A*.....	0	0	>18.4	0.3	>16.6	0.3	11.7	0.5		
S2+Sgr A*.....	0.02	0.04	15.36	0.1	14.01	0.1	11.12	0.1	1.3	2.9
S1.....	-0.05	-0.18	16.1	0.1	14.79	0.12	12.86	0.2	1.3	1.9
S4.....	0.25	0.13	15.74	0.1	14.42	0.1	12.60	0.13	1.3	1.8
S12.....	-0.08	0.27	16.88	0.1	15.58	0.1	13.99	0.15	1.3	1.6
S9.....	0.17	-0.34	16.55	0.1	15.17	0.12	12.95	0.1	1.4	2.2
S10.....	0.050	-0.37	15.78	0.1	14.23	0.1	12.14	0.1	1.5	2.1
S8.....	0.36	-0.24	15.89	0.1	14.52	0.1	12.63	0.12	1.4	1.9
S5.....	0.46	0.10	16.92	0.1	15.44	0.12	13.29	0.2	1.5	2.2
S7.....	0.51	-0.03	16.70	0.11	15.34	0.14	12.63	0.13	1.4	2.7
S11.....	0.15	-0.55	15.78	0.1	14.43	0.1	12.43	0.12	1.4	2.0
IRS 16SWNW.....	0.53	-0.43	14.88	0.1	13.41	0.1	11.65	0.1	1.5	1.8
	0.51	0.45	16.37	0.1	15.13	0.1	13.20	0.11	1.2	1.9

Current models of the accretion flow predict that the infrared emission predominantly comes from the tail of the radio/submillimeter synchrotron emission (Melia & Falcke 2001; Narayan, Yi, & Mahadevan 1995; Falcke & Biermann 1999; Markoff et al. 2001; Liu & Melia 2002; Hawley & Balbus 2002). The infrared spectral energy distribution is inverted, and the L' -band data provide valuable constraints on the innermost parts of the accretion zone. Our deduced L' excess flux density is significantly larger than the values predicted by the various theoretical “quiescent state” models (Markoff et al. 2001; Liu & Melia 2002). The model that comes closest (within a factor of a few) is the jet-disk model of Markoff et al. (2001). Enhanced mid-IR emission at about the observed level is theoretically predicted to occur during flares, such as observed at X-rays (Baganoff et al. 2001).

Alternatively, the mid-IR emission may come from dust in the accretion flow onto the black hole that is heated by the hot, luminous O star S2. We show in Appendix B that dust in the accretion flow onto Sgr A* can be heated to sufficiently high temperature by the ultraviolet radiation from S2 and can account for the L' excess if

$$(\dot{M}f_{\text{dust}})_{R=0.002 \text{ pc}} \sim 2 \times 10^{-7} (M_{\odot} \text{ yr}^{-1}). \quad (4)$$

Here \dot{M} is the mass accretion rate onto the black hole and f_{dust} is the abundance of dust in the flow, relative to that in the interstellar medium. This mass accretion rate is in good agreement with a recent estimate ($10^{-7} M_{\odot} \text{ yr}^{-1}$) based on the $\sim 10\%$ linear polarization of Sgr A* in the millimeter range (Bower et al. 2003). The estimated mass accretion rate also agrees with recent theoretical models of the Sgr A* spectral energy distribution, including its X-ray emission (Liu & Melia 2002; Markoff et al. 2001) but is 2–3 orders of magnitude lower than earlier models based on advection-dominated accretion flows (ADAFs; Narayan et al. 1995) or Bondi flows (Melia 1992).

A definite test of whether the observed L' -band excess is caused by S2 heating the accretion flow or by (variable) emission from the black hole flow itself will come from multiepoch observations that we began on the VLT in the spring of 2003. The “UV heating” model predicts that the excess emission should continue to be centered on S2 but should become dimmer as the star moves away from Sgr A*. The Sgr A* model in turn predicts that the mid-IR excess emission should be centered on the radio source, probably be polarized, and strongly vary with time. First observations taken in 2003 March appear to favor that the source of the excess emission is Sgr A* itself.

4. DISCUSSION: THE ORIGIN OF THE EARLY-TYPE STARS IN THE CUSP

In this section we discuss how the massive and apparently young stars discussed in the last section may have come to reside in the dense central environment around the central massive black hole. The key questions are whether they can have formed in situ, or whether otherwise they might have migrated there from farther out. We discuss different possibilities that have been proposed and discussed in the literature during the last decade. We believe that our new dynamical data make a good case that a cloud collision mechanism is the most likely possibility for the formation of massive stars at $1''$ – $10''$ from the center, while a collision-

merger model of smaller stars may be the most likely model for the formation of the S-stars in the innermost region around the black hole.

First, the blue supergiants and Wolf-Rayet stars $1''$ – $10''$ from the center, and even more clearly the S-stars in the Sgr A* cluster, cannot have migrated through two-body processes to their present location from large radii. The relaxation time of stars of mass m is given by (e.g., Alexander 2002)

$$t_r(m) = 10^{8.2} M_3^{3/2} R_{10}^{-0.13} m_{10}^{-1} \left[\ln \left(\frac{N_*}{12} \right) \right]^{-1} \text{ (yr)}, \quad (5)$$

where M_3 is the mass enclosed within radius R_{10} (in units of $10''$ or 0.38 pc) in units of $3 \times 10^6 M_{\odot}$, m_{10} is the stellar mass in units of $10 M_{\odot}$, and N_* is the number of stars. In the central $10''$ the relaxation time is approximately independent of radius (for a cusp of radial exponent $\alpha = 1.4$). This needs to be compared to the (main sequence) stellar lifetime (Genzel et al. 1994; Cox 2000),

$$t_{\text{ms}}(m) \begin{cases} 10^{7.3} m_{10}^{-2.5} \text{ (yr)}, & m_{10} \leq 0.9, \\ 10^{7.2} m_{10}^{-1.5} \text{ (yr)}, & m_{10} > 0.9. \end{cases} \quad (6)$$

Clearly, stars more massive than about $2.5 M_{\odot}$ cannot have formed outside the central region and then mass-segregated through two-body relaxation to the central few arcseconds.

4.1. Current Star Formation in the Minispiral?

One possibility is that massive stars form continuously outside the dense central region and rapidly pass through the center on highly elliptical orbits. For instance, the northern arm of the minispiral appears to be on such a trajectory. The dusty sources associated with the gas might be candidates for young stars formed in and still embedded in their parental gas clouds. Becklin et al. (1978) were the first to propose that compact mid-IR bright sources in the minispiral, such as IRS 1, 2/13, 5, and 10, are compact H II regions surrounding intrinsically luminous (and hot) stars. Gezari, Dwek, & Varosi (1994) showed that these sources and also IRS 21 are local dust temperature peaks in the minispiral and, therefore, must contain local luminosity sources. Based on the dust-excess, featureless, near-IR spectra of the “minispiral sources,” Krabbe et al. (1995) and Ott et al. (1999) proposed that they might be young, recently formed stars embedded in the minispiral. IRS 1, 5, 10, and 21 are, however, offset from the emission and temperature peaks of the diffuse dust in the minispiral ridge (Cotera et al. 1999). Tanner et al. (2002) carried out detailed Keck observations of the near- and mid-IR emission of IRS 21 and proposed that this source is a luminous post-main-sequence (Wolf-Rayet) star. In the model of Tanner et al., IRS 21 is just fortuitously near the gas/dust of the minispiral. Its extended dust emission is a bow shock created by the motion of the star into the minispiral. Comparison of the stellar proper motions of these minispiral sources with the proper motions of the gas derived from VLA images (Yusef-Zadeh, Roberts, & Biretta 1998; Zhao & Goss 1999) can distinguish between the “embedded young star” and “older stars moving through gas/dust” hypotheses. The results of this comparison are shown in Figure 18.

The left panel of Figure 18 shows a gray-scale 1.3 cm radio image of the northern/eastern arms and the bar (Zhao

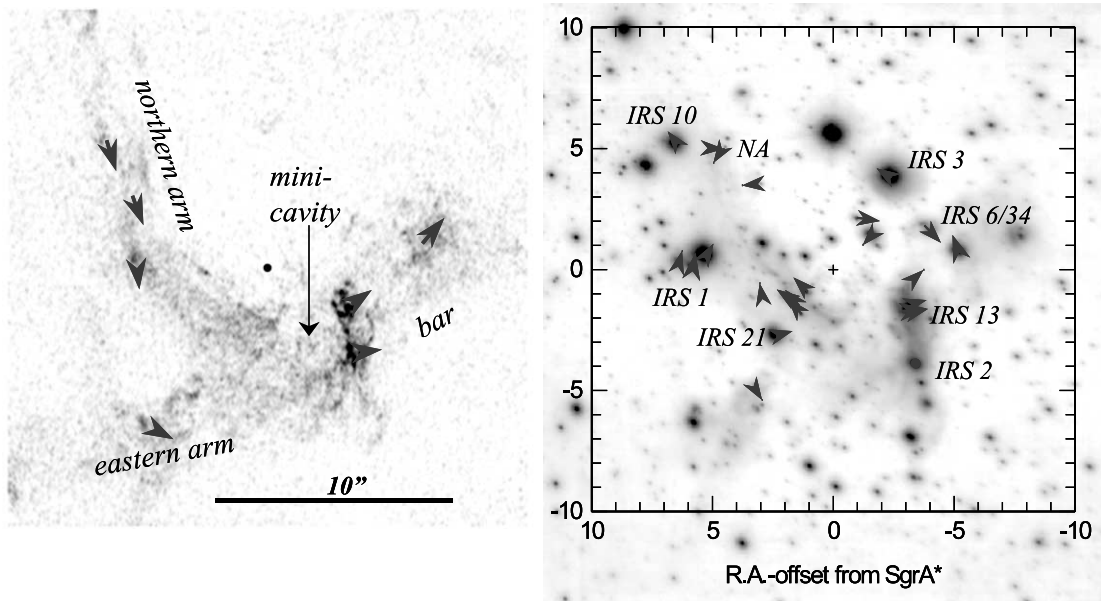


FIG. 18.—Comparison of proper motions of gas and stars near the gaseous minispiral. *Left*: False color image of 1.3 cm radio continuum emission from Zhao & Goss (1998; 0".1 resolution), with arrows denoting the proper motions of gas components in the northern and eastern arms, and the bar plus minicavity regions of the minispiral (Yusef-Zadeh et al. 1998). The ionized gas in the northern arm/bar streams from the north (and behind) anticlockwise around Sgr A*, and streams outward to the west and front of the radio source. *Right*: NAOS/CONICA L' image (logarithmic gray scale), with arrows denoting the proper motions of stars with L' excess ($K-L' \geq 2$). With the exception of several dusty stars in/near IRS 13, other dusty objects apparently associated with the minispiral show proper motions that are distinctly different from that of the gas. These stars likely are interacting with and passing through the gas and dust of the minispiral but are not physically associated with it.

& Goss 1998), along with some of the gas proper motion vectors deduced by Yusef-Zadeh et al. (1998). The bulk of the ionized gas in the northern arm, minicavity, and bar is streaming south-southwest in a counterclockwise pattern on the sky and in the general sense of Galactic rotation (Lacy, Achtermann, & Serabyn 1991; Yusef-Zadeh et al. 1998). The gas streamers are in a plane, which is inclined $\sim 65^\circ$ with respect to the line of sight (Lacy et al. 1991; Vollmer & Duschl 2000). The right panel shows the proper-motion vectors of those stars in the Ott et al. sample that are not late-type stars, are dusty, i.e., have a significant L' excess ($K-L' = 2$), and have $K < 15$. These proper motions clearly demonstrate that most of the dusty minispiral L' stars do not share the motion of the minispiral gas. As proposed by Tanner et al. (2002), they just happen to move through and interact with the minispiral gas/dust. IRS 10 (west), several sources in the northern arm (NA), IRS 1, IRS 21, the IRS 16 sources, and sources in/near the bar (IRS 29/3/34) have proper motions that are inconsistent with the gas streaming vectors. In particular, the proper motion of IRS 21 is fully consistent with the Tanner et al. (2002) bow shock model. One of the northern arm sources moving eastward into the northern arm in fact is associated with a bow shock structure on the L' map (source NA moving eastward in the right panel). In addition, the spectroscopic data of T. Ott et al. (2003, in preparation) indicate that several of the dusty sources indeed are late-type, carbon-rich, Wolf-Rayet (WC) stars. We thus conclude that there is little evidence for current star formation in the minispiral gas streamers. The only possible case for dusty stars moving along with the gas of the minispiral is the IRS 13 complex. At the northern tip of the IRS 13 complex is a group of compact L' sources with a very large $K-L'$ excess, which may be candidates for deeply embedded and very young stars embedded in the bar

(A. Eckart et al. 2003, in preparation). The IRS 13 complex may thus be a plausible candidate region for recent star formation in the gas streamers. It is not clear, however, whether IRS 13/2 is actually part of the large-scale northern arm structure, or whether it is a separate dynamical feature in the bar (Vollmer & Duschl 2000).

If massive stars are forming frequently in dense gas streamers when outside the central parsec and then rapidly move through the central region, one would expect ~ 100 times as many massive stars outside the central region as in the central parsec. Only a few such stars have so far been found in the central 10 pc, although complete surveys have been shallow (Figer 1995) and deeper searches were confined to known compact H II regions (Cotera et al. 1999). In the recent deeper spectroscopic work by T. Ott et al. (2003, in preparation), no new emission-line stars have been detected outside the known “starburst region” of diameter $\sim 25''$. With the possible exception of IRS 13, a model in which massive stars are formed outside the dense central region and just pass through the center on highly elliptical orbits does not seem to be supported by the observations. Most of the bright dusty sources associated with the minispiral are not embedded “protostars.”

4.2. Infall of Young, Massive Star Clusters

To overcome the long timescales implied by two-body relaxation, Gerhard (2001) proposed that a young star cluster spiraled into the nucleus through dynamical friction and made it to the central parsec before it was tidally disrupted there. Portegies Zwart, McMillan, & Gerhard (2003) have shown by more detailed numerical simulations that the Gerhard scenario is feasible. It requires that such a cluster has to be very massive ($\geq 10^4 M_\odot$) and dense (and thus

compact: 0.2–0.4 pc) to spiral into the center within the lifetime of its O stars (a few Myr), core-collapse, and arrive there before dissolving completely. The dynamical friction time scales inversely with the cluster mass so that a 10^5 – $10^6 M_\odot$ cluster can spiral into the center from parsec-scale distances in a few Myr. The two known (nonnuclear) young star clusters in the central 30 pc, the Quintuplet and Arches clusters, have a diameter of ~ 0.4 pc and a mass of a few $10^4 M_\odot$ (extrapolating the observed stellar content to $1 M_\odot$; Figer 2003). The N -body simulations by Portegies Zwart et al. (2003) show that a cluster of mass $6 \times 10^4 M_\odot$ and diameter less than 0.3 pc could make it into the central parsec within the available time from an initial radius of 4–5 pc, but not from farther out. The inspiraling cluster maintains its orbital angular momentum direction, and the tidally disrupted final remnant of such a cluster resembles a thin rotating disk, similar to what we observe. However, the final radius reached by the dissolving cluster in the simulation by Portegies Zwart et al. (2003) is 1–2 pc, significantly larger than the characteristic radius of either one of the two rotating disks of young stars (0.1–0.4 pc). Further, there is presently no observational evidence for such dense ($> 10^6 \text{ cm}^{-3}$), compact, and massive molecular concentrations within a few parsecs of the nucleus (Mezger et al. 1996). Several molecular clouds of more than $10^5 M_\odot$ are located at distances of more than 10 pc from the center (Mezger et al. 1996). At that radius the tidal requirements are much reduced, although a cluster that formed efficiently from such a cloud must still have been very compact to rapidly core-collapse and thus make it intact into the central region. Finally, the fact that we see two such disks, with different angular momenta, requires that two massive clusters must have fallen in at about the same time (and none later). This is statistically unlikely. We conclude that the “infalling cluster” scenario, while attractive, fails to match the specific properties of the two rotating disks of young stars in the Galactic center.

4.3. *In Situ Formation from Dense Gas*

The third possibility is that stars formed in situ from cloud collapse, following the infall of (a) dense gas cloud(s). Several molecular and ionized gas clouds are detected in the central parsec, several with large radial velocities, and a few even with the correct (and anti-Galactic) angular momentum (Jackson et al. 1993; Lacy et al. 1991; Genzel et al. 1996). The mass in the presently observed circumnuclear molecular material is several $10^4 M_\odot$. This is amply sufficient to account for the massive star content in the 2–7 Myr starburst component $1''$ – $10''$ from the center (one to a few thousand solar masses; Krabbe et al. 1995). It may also be sufficient to account for formation of lower mass stars with a Salpeter-like mass function if the star formation efficiency is sufficiently high. For self-gravity in interstellar clouds to overwhelm the tidal shear and create 10^3 – $10^4 M_\odot$ of stars in the 2–7 Myr starburst component, however, requires gas densities of $(5\text{--}10) \times 10^9 \text{ hydrogen atoms cm}^{-3}$. This is several thousand times greater than the density of gas clumps currently found in the atomic and molecular gas clouds in the central 1–2 pc [$n(\text{H}, \text{H}_2) \leq 10^6 \text{ cm}^{-3}$; Jackson et al. 1993; Genzel et al. 1994]. For the S-stars bound to the black hole within the central arcsecond, the required gas densities are even more extreme ($\geq 10^{13.5} \text{ cm}^{-3}$). Hence, gas clumps naturally occurring in known circumnuclear gas would have to be compressed very substantially before they could

collapse to form stars. A cloud-cloud collision and shocks resulting from it, as well as the action on that gas by stellar winds in the central region, may be possible agents for achieving such compressions (Morris 1993). Some evidence for large compression and the action of winds comes from high-resolution radio maps (Yusef-Zadeh et al. 1998) and the new NAOS/CONICA L' images (Figs. 1 and 18; Clénet et al. 2003). The L' image exhibits sharp (diameter $\leq 0''.1$) filaments, plausibly caused by the interaction of the minispiral streamers with the outflows and winds from the central few arcseconds.

There are no published simulations of such a cloud collision near a black hole, but it is clear qualitatively that the cooling, postshock material would have lost a lot of its original angular momentum and settled into a disk circulating around the hole. Subsequently, the disk could lose additional angular momentum through magnetic friction (Hawley & Balbus 2002) or interaction with the stellar winds in the central parsec. Through that angular momentum transport the gas disk could then slowly contract and eventually become dense enough in its inner parts to form stars (e.g., Levin & Boloborodov 2003; Nayakshin, Cuadra, & Sunyaev 2003).

We cannot quantitatively evaluate this scenario at the present time but conjecture that it has two natural and critical features matching our new observations. First, a cloud collision is a sudden compression that may trigger a burst of star formation. Second, the two colliding clouds would plausibly move in rather different directions and would be compressed at the same time, thus leading to coeval star formation in the postshock gas of both clouds. If the splashing shocked gas retains some memory of the original cloud momenta, the gas might settle into two counterrotating disks. We therefore think that the colliding clouds model is qualitatively very attractive for explaining the two counterrotating and coeval massive star disks $1''$ – $10''$ from Sgr A*. Obviously, a realistic hydrodynamic simulation of such a cloud collision in the gravitational potential of a massive black hole should be carried out for testing the notion that a cloud collision can lead to two separate rotating disks. If that turns out to not be the case, one would have to resort to a model in which two clouds happened to fall into the center at the same time and then gradually lost angular momentum and contracted until they could form stars. This scenario suffers from the same problem of low statistical probability as that of the two inspiraling star clusters.

4.4. *The S-Stars near Sgr A*: Super-Blue Stragglers?*

Another possibility is that the massive stars are continuously formed through mergers of lower mass stars. In this case the massive early-type stars may be old stars that have been rejuvenated in the very dense environment of the cusp (Morris 1993; Genzel et al. 1994; Lee 1994; Alexander 2002). The probability of massive stars to being formed in this way can be qualitatively assessed by comparing the collision timescale between stars of different masses with their lifetime. Since the collisional timescale increases but the stellar lifetime decreases with mass, the maximum stellar mass formed in a merger tree occurs roughly when the two timescales are equal. As shown analytically in Appendix A, $10 M_\odot$ stars can plausibly be formed in this way in the innermost cusp, within a few tenths of an arcsecond of Sgr A*, if the merger efficiency in high-velocity collisions is high and if

angular momentum of the rapidly rotating merger is efficiently removed. The S-stars in the Sgr A* cluster may thus be collisional products. They may be “super-blue stragglers,” similar to but much more massive than those found in globular clusters (Bailyn 1995). However, the more massive He I emission-line stars (30–100 M_{\odot}) 1''–12'' from Sgr A* clearly cannot have been formed this way, in agreement with the more detailed Fokker-Planck calculations of Lee (1994).

Another predicted effect of stellar collisions in the cusp is the destruction of late-type giants (Alexander 1999, 2002). We show in Appendix A that within the central $\sim 1''$, near-central collisions occur between late-type giants and solar mass stars within a giant’s lifetime. If such collisions permanently destroy the giant’s envelope, one would expect that the density of late-type giants decreases in the central few arcseconds. We have shown above (Fig. 7) that the fraction of $K_s \leq 15$ giants in fact appears lower within the central 2'', which is in agreement with the collider model and the earlier conclusions of Alexander (1999).

5. CONCLUSIONS

We have presented a new analysis of the properties of the star cluster in the central 10'' of our Milky Way, based on deep near-IR adaptive optics imaging with NAOS/CONICA on the ESO VLT and a new database of stellar proper motions. Our main results can be summarized as follows:

1. The faint stars form a power-law cusp centered on the massive black hole Sgr A*. Our observations resolve the long-standing paradox of why the infrared light distribution peaks away from the position of Sgr A*. The stellar density in the central arcsecond exceeds $3 \times 10^7 M_{\odot} \text{ pc}^{-3}$. Stellar collisions are expected to be frequent.

2. The shape of the K -band luminosity function of the central parsec is consistent with the properties of an old, metal-rich star cluster, with an admixture of massive young stars.

3. The K -band luminosity function, faint number counts, and late-type star fraction in the central few arcseconds suggest that stellar content and properties change significantly in the dense innermost cusp. To the $K \leq 15$ mag limit reached by spectra and proper motions, the cusp is dominated by massive, early-type stars.

4. The $K \leq 15$ early-type stars, similar to the brightest He I emission-line stars studied over the past decade, are dynamically unrelaxed and thus must be young. Most of the early-type stars in the central 10'' appear to reside in two fairly thin rotating disks. These disks orbit the black hole, are inclined at large angles, and counterrotate with respect to each other. The two star disks have essentially the same stellar content and thus must have formed coevally, within less than 1 Myr.

5. Of the various proposals as to how the massive stars have made it into the central 1''–10'', our new observations, and in particular the pattern of two coeval rotating disks of massive stars, now appear to favor in situ formation following the collision of gas clouds. We propose that two dense and moderately massive (a few 10^3 to $10^4 M_{\odot}$) interstellar clouds fell into the central parsec and collided there about 5–8 million years ago. The shock-compressed gas then settled into two counterrotating disks that probably subsequently lost further angular momentum, moved inward, and finally became gravitationally unstable and formed stars.

6. In contrast to the massive stars at $p = 1''$ –10'', the early-type stars in the Sgr A* cluster (the S-stars) in our opinion are most likely formed as a result of collisions and mergers of lower mass stars, in analogy to the blue straggler phenomenon in globular clusters.

7. The star closest to the black hole in 2002, S2, exhibits a mid-infrared excess. We propose that this excess is caused either by infrared emission from the accretion region around Sgr A* itself or by the interaction of the star’s UV light with dust in the accretion flow onto the black hole. In the latter case, the lower limit to the accretion rate 10–40 mas (1400–5700 Schwarzschild radii) from the hole is about $10^{-7} M_{\odot} \text{ yr}^{-1}$.

We are grateful to all members of the NAOS/CONICA team (from MPIA, MPE, Observatoire de Grenoble, Observatoire de Meudon, ONERA, and ESO-Garching) and the ESO-Paranal staff whose hard and dedicated work made these observations possible. In particular, we thank N. Ageorges, K. Bickert, W. Brandner, E. Gendron, M. Hartung, N. Hubin, C. Lidman, A.-M. Lagrange, A. F. M. Moorwood, C. Röhrle, G. Rousset, and J. Spyromilio. We thank C. Bailyn, M. Davies, and A. Sills for discussions on the properties of blue stragglers, C. McKee for comments on dust destruction in fast shocks, and Y. Levin, A. Beloborodov, and S. Nayakshin for interesting discussions about the stars in the black hole environment. We thank M. Goss for making available to us his high-resolution VLA 1.3 cm data. Our work is in part based on observations obtained at the Gemini Observatory, which is operated by the Association of Universities for Research in Astronomy, Inc., under a cooperative agreement with the NSF on behalf of the Gemini partnership: the National Science Foundation (United States), the Particle Physics and Astronomy Research Council (United Kingdom), the National Research Council (Canada), CONICYT (Chile), the Australian Research Council (Australia), CNPq (Brazil), and CONICET (Argentina). Collaborative research between MPE and Tel Aviv University is supported by the German-Israeli Foundation (grant I-0551-186.07/97). T. A. is supported by GIF grant 2044/01, Minerva grant 8484, and a New Faculty grant by Sir H. Djangoly, CBE, London, UK.

APPENDIX A

BUILDUP OF MASSIVE STARS BY COLLISIONS AND MERGERS

Following Alexander (1999), the timescale for the collision of a star of mass m_1 with another star of mass m_2 (M_\odot), with stellar radii r_1 and r_2 , at an average radius R (arcsec) from Sgr A* can be expressed as

$$t_c = \left\{ 4\sqrt{\pi}\sigma C_g n_2 (x r_1 + r_2)^2 \left[1 + \frac{C_f G(m_1 + m_2)}{C_g 2(x r_1 + r_2)\sigma^2} \right] \right\}^{-1}, \quad (\text{A1})$$

where the normal geometric cross section (g) and gravitational focusing (f) terms have been modified by average correction factors C_g and C_f to account for orbit averaging. The factor x describes how off-center the collision is relative to the center of star 1 ($x = 0$ is central, $x = 1$ is grazing). We assume that the stellar density distribution is described by

$$n_*(R) = \frac{\rho_*(R)}{\langle m \rangle} = 2.2 \times 10^7 R_1^{-1.4} (M_\odot \text{ pc}^{-3}), \quad (\text{A2})$$

where $\langle m \rangle = 1.3 M_\odot$ is the average stellar mass for a Salpeter mass function between 0.5 and 20 M_\odot and R_1 is the separation from Sgr A* in arcseconds. To normalize the last equation, we have taken a broken power law density distribution ($\rho \propto R^{-\alpha}$) with an exponent $\alpha = 1.4$ inside $10''$ and 2 outside and with the mass normalization discussed in § 3.2 (Genzel et al. 1996). The density of collision partner n_2 then can be expressed as $n_2 = n_* f(m_2)$, where $f(m)$ is the fraction of stars in mass bin m . The one-dimensional velocity dispersion scales with radius from the black hole of mass $M_{\text{BH}} = 3 \times 10^6 M_\odot$ as (Alexander 1999)

$$\sigma(R) = \frac{v_c}{\sqrt{1 + \alpha}} = \sqrt{\frac{GM_{\text{BH}}}{(1 + \alpha)R}} = 364 R_1^{-1/2} (\text{km s}^{-1}). \quad (\text{A3})$$

For main-sequence stars of mass m (M_\odot), we take the standard radius-mass relationship (Cox 2000)

$$r(m) = 1.03 m^{0.64} (R_\odot). \quad (\text{A4})$$

For $\alpha = 1.4$, Alexander (1999) finds $C_g \sim 2.08$ and $C_f \sim 1.36$, which reflects the fact that $\sim 80\%$ of the cusp stars are bound to the black hole and thus that they spend significant time at $R < \langle R \rangle$, where the collisions are more frequent. For collisions to be effective, they have to occur within the lifetime of the star m_1 . We take the mass dependence of the main-sequence lifetime to be (Genzel et al. 1994)

$$t_{\text{ms}}(m) = \begin{cases} 10^{9.8} m^{-2.5} (\text{yr}), & m_{10} \leq 0.9, \\ 10^{8.7} m^{-1.5} (\text{yr}), & m_{10} > 0.9. \end{cases} \quad (\text{A5})$$

Collisions are effective for forming a star of mass m_3 from the merger of m_1 and m_2 if

$$P(m_3, m_2, m_1) = \frac{\tau_{\text{ms}}(m_3)}{t_c(m_1, m_2)} \geq 1. \quad (\text{A6})$$

For grazing collisions of two main-sequence stars, the collision time is

$$t_c(m, m) = 4 \times 10^9 m^{-1.28} R_1^{1.9} (1 + 0.5 m^{0.36} R_1)^{-1} f(m)^{-1} (\text{yr}). \quad (\text{A7})$$

For $m = 1 M_\odot$, the radius R_c within which $P \geq 1$ then is about $0''.6$. If the merging efficiency is high for grazing collisions (see references in Genzel et al. 1994), R_c is then also the radius within which many $1 M_\odot$ stars continuously merge into $2 M_\odot$ stars. The S-sources require collisions and merging of more massive stars, however. For $m = 5$ ($m_3 = 10 M_\odot$ merger product), R_c is about $0.3 f(5)^{0.53}$, or $\geq 0''.1$ for $f(5) \geq 0.1$. Obviously, a more realistic calculation of the entire merger tree is desirable, but our estimate already suggests that the merger model predicts a significant number of $\sim 10 M_\odot$ stars to occur within the Sgr A* cluster zone. Our estimates obviously require that the merging efficiency be high and that the angular momentum of the (initially) rapidly rotating merger remnant be removed quickly. Very little is known theoretically about the merging efficiencies in the high-velocity collision domain that characterizes the Galactic center, but naively one would expect that they should be low. However, recent SPH simulations of stellar collisions at high velocities by one of us (T. A.) suggest that merging efficiencies may be surprisingly large under a fairly wide range of conditions. How angular momentum is transported away in stellar mergers is not understood quantitatively (Sills & Bailyn 1999; Sills et al. 2001). Qualitatively, it is thought that some sort of magnetic breaking, either through a wind/outflow or through a locked circumstellar disk, is efficient (Sills et al. 2001). Blue stragglers are obviously formed in significant numbers in globular clusters, indicating that nature has found a way to solve the angular momentum problem (Bailyn 1995). In the one case where a rotation velocity is measured (Shara, Saffer, & Livio 1997), the rotation is moderately fast [$v_{\text{rot}} \sin(i) = 155 \text{ km s}^{-1}$] but significantly below breakup. The deduced rotation velocity of S2 (224 km s^{-1}) is also not unusual for a normal late-O star (Ghez et al. 2003).

Another predicted effect of the collision model in the cusp (Alexander & Livio 2001; Alexander & Kumar 2001; Alexander 2002; Alexander & Morris 2003) is the destruction of late-type giants. Again we apply the above equations with $m_1 = m_g \sim 2 M_\odot$, $m_2 = \langle m \rangle$ and assume that near-central collisions ($x \sim 0.25$) between a giant and a low-mass dwarf star result in the permanent destruction of the giant's envelope (Davies et al. 1998; Alexander 1999). Bright red giants (M1–K5, $K_s \sim 12\text{--}14$)

have a lifetime of about 10% of τ_{ms} and a radius of 20–80 R_{\odot} (Cox 2000). The collision time then is

$$t_c(g, \langle m \rangle) \sim 9 \times 10^7 R_1^2 (1 + 0.1 R_1)^{-1} f(\langle m \rangle)^{-1} \text{ (yr)} , \quad (\text{A8})$$

and $P \geq 1$ occurs within $R_c \sim 1''/2$ for a 50 R_{\odot} giant. In this regime R_c scales approximately with $(x r_g)^2$ so that destruction occurs at even greater radii for the even larger AGB stars and, if the envelope is destroyed, at more off-center collisions. We have shown above (Fig. 7) that the fraction of $K_s \leq 15$ giants decreases within the central 2'', in good agreement with the collider model and the earlier conclusions of Alexander (1999).

APPENDIX B

HEATING OF DUST IN THE ACCRETION FLOW BY UV RADIATION FROM S2

We show here that the mid-IR excess emission of S2/Sgr A* may come from dust in the accretion flow (onto the black hole) that is heated by the hot and luminous O star S2. The UV dust optical depth of this flow can be estimated from

$$\tau_{\text{UV}} = f_{\text{dust}} \left(\frac{\dot{M} r / 4\pi R^2 v \mu}{6.3 \times 10^{20} \text{ cm}^{-2}} \right) . \quad (\text{B1})$$

Here \dot{M} is the mass accretion rate onto Sgr A*, R ($\sim 2 \times 10^{-3}$ pc) is the distance of S2 from Sgr A*, μ is the mean molecular weight (3.4×10^{-24} g), v is the velocity of the accretion flow, r is the radius of the dust column from S2, and f_{dust} is the fraction of dust (relative to the normal interstellar medium) that is not destroyed because of the accretion shock in the hot accretion flow near S2. The temperature the dust particles attain is given from the heating-cooling balance,

$$T_d(r) \sim T_0 \left(\frac{L_{\text{UV}}}{L_0} \right)^{1/(4+\beta)} \left(\frac{r}{r_0} \right)^{-2/(4+\beta)} . \quad (\text{B2})$$

For dust particles with wavelength-dependent extinction efficiency $Q(\lambda) = Q(\lambda_0)(\lambda/\lambda_0)^{-\beta}$ and normal interstellar dust parameters, $\beta = 1$, $T_0 = 82$ K, $L_0 = 10^5 L_{\odot}$, and $r_0 = 3 \times 10^{17}$ cm (Scoville & Kwan 1976). For simplicity we assume further that the emission at λ is dominated by those dust particles whose temperature at r is equal to the Wien temperature [$T_{\text{Wien}}(L') = 710$ K]. For a late-O star the UV luminosity is about half of the bolometric luminosity, such that $r(T_{\text{Wien}}(L')) = 10^{15}$ cm. The emitted flux density of this hot dust cloud around the O/B star then is

$$S(L') = 17.5 r_{15}^2 \tau_{\text{UV}} \text{ (Jy)} , \quad (\text{B3})$$

for an assumed 8 kpc distance to the Galactic center. Comparison to the observed flux density implies $\tau_{\text{UV}} \sim 1.7 \times 10^{-3}$. For $v = 10^3$ km s $^{-1}$, we find

$$(\dot{M} f_{\text{dust}})_{R=0.002 \text{ pc}} \sim 2 \times 10^{-7} (M_{\odot} \text{ yr}^{-1}) . \quad (\text{B4})$$

Dust destruction in fast shocks is mostly due to sputtering. It strongly depends on the preshock gas density and leads to a deficiency of small grains (Dwek, Foster, & Vancura 1996). For the gas densities in the pre-accretion shock region in the Galactic center (between 0.1 and 10 cm $^{-3}$ at $R = 1''$), we estimate from the models of Dwek et al. that 15%–70% of the dust is destroyed.

REFERENCES

- Alexander, T. 1999, *ApJ*, 527, 835
 ———. 2002, in *The Galactic Black Hole*, ed. H. Falcke & F. W. Hehl (Bristol: IOP), 246
 Alexander, T., & Kumar, P. 2001, *ApJ*, 549, 948
 Alexander, T., & Livio, M. 2001, *ApJ*, 560, L143
 Alexander, T., & Morris, M. 2003, *ApJ*, 590, L25
 Alexander, T., & Sternberg, A. 1999, *ApJ*, 520, 137
 Allen, D. A. 1994, in *The Nuclei of Normal Galaxies*, ed. R. Genzel & A. I. Harris (NATO ASI Ser. C, 445; Dordrecht: Kluwer), 293
 Allen, D. A., Hyland, A. R., & Hillier, D. J. 1990, *MNRAS*, 244, 706
 Allen, D. A., & Sanders, R. H. 1986, *Nature*, 319, 191
 Backer, D. C., & Sramek, R. A. 1999, *ApJ*, 524, 805
 Baganoff, F. K., et al. 2001, *Nature*, 413, 45
 Bahcall, J. N., & Wolf, R. A. 1976, *ApJ*, 209, 214
 ———. 1977, *ApJ*, 216, 883
 Bailyn, C. D. 1995, *ARA&A*, 33, 133
 Becklin, E. E., Mathews, K., Neugebauer, G., & Willner, S. P. 1978, *ApJ*, 219, 121
 Blum, R. D., Sellgren, K., & DePoy, D. L. 1996a, *ApJ*, 470, 864
 ———. 1996b, *AJ*, 112, 1988
 Bower, G. C., Wright, M. C. H., Falcke, H., & Backer, D. C. 2003, *ApJ*, 588, 331
 Brandner, W., et al. 2002, *Messenger*, 107, 1
 Catchpole, R. M., Whitelock, P. A., & Glass, I. S. 1990, *MNRAS*, 247, 479
 Chakrabarty, D., & Saha, P. 2001, *AJ*, 122, 232
 Cl  net, Y., et al. 2003, *A&A*, submitted
 Cotera, A. S., Simpson, J. P., Erickson, E. F., Colgan, S. W. J., Burton, M. G., & Allen, D. A. 1999, *ApJ*, 510, 747
 Cox, A. N. 2000, *Allen's Astrophysical Quantities* (Berlin: Springer)
 Davidge, T. J., Simons, D. A., Rigaut, F., Doyon, R., & Crampton, D. 1997, *AJ*, 114, 2586
 Davies, M. B., & Benz, W. 1991, *ApJ*, 381, 449
 Davies, M. B., Blackwell, R., Bailey, V. C., & Sigurdsson, S. 1998, *MNRAS*, 301, 745
 Doleman, S. S., et al. 2001, *AJ*, 121, 2610
 Dwek, E., Foster, S. M., & Vancura, O. 1996, *ApJ*, 457, 244
 Eckart, A., & Genzel, R. 1996, *Nature*, 383, 415
 ———. 1997, *MNRAS*, 284, 576
 Eckart, A., Genzel, R., Hofmann, R., Sams, B. J., & Tacconi-Garman, L. E. 1993, *ApJ*, 407, L77
 ———. 1995, *ApJ*, 445, L23
 Eckart, A., Genzel, R., Ott, T., & Sch  del, R. 2002, *MNRAS*, 331, 917
 Eckart, A., Ott, T., & Genzel, R. 1999, *A&A*, 352, L22
 Falcke, H., & Biermann, P. L. 1999, *A&A*, 342, 49
 Figer, D. F. 1995, Ph.D. thesis, UCLA
 ———. 2003, in *IAU Symp. 212, A Massive Star Odyssey, from Main Sequence to Supernova*, ed. K. A. van der Hucht, A. Herrero, & C. Esteban (San Francisco: ASP), in press
 Figer, D. F., Kim, S. S., Morris, M., Serabyn, E., Rich, R. M., & McLean, I. S. 1999, *ApJ*, 525, 750
 Figer, D. F., Najarro, F., Morris, M., McLean, I. S., Geballe, T. R., Ghez, A., & Langer, N. 1998, *ApJ*, 506, 384

- Figer, D. F., et al. 2000, *ApJ*, 533, L49
- Forrest, W. J., Shure, M. A., Pipher, J. L., & Woodward, C. A. 1987, in *AIP Conf. 155, The Galactic Center*, ed. D. C. Backer (New York: AIP), 153
- Genzel, R. 2001, in *ASP Conf. Ser. 228, Dynamics of Star Clusters and the Milky Way*, ed. S. Deiters, B. Fuchs, R. Spurzem, A. Just, & R. Wielen (San Francisco: ASP), 291
- Genzel, R., Eckart, A., Ott, T., & Eisenhauer, F. 1997, *MNRAS*, 291, 219
- Genzel, R., Hollenbach, D., & Townes, C. H. 1994, *Rep. Prog. Phys.*, 57, 417
- Genzel, R., Pichon, C., Eckart, A., Gerhard, O., & Ott, T. 2000, *MNRAS*, 317, 348
- Genzel, R., Thatte, N., Krabbe, A., Kroker H., & Tacconi-Garman, L. E. 1996, *ApJ*, 472, 153
- Gerhard, O. 2001, *ApJ*, 546, L39
- Gezari, D., Dwek, E., & Varosi, F. 1994, in *The Nuclei of Normal Galaxies*, ed. R. Genzel & A. I. Harris (NATO ASI Ser. C, 445; Dordrecht: Kluwer), 343
- Gezari, S., Ghez, A. M., Becklin, E. E., Larkin, J., McLean, I. S., & Morris, M. 2002, *ApJ*, 576, 790
- Ghez, A. M., Klein, B. L., Morris, M., & Becklin, E. E. 1998, *ApJ*, 509, 678
- Ghez, A. M., Morris, M., Becklin, E. E., Tanner, A., & Kremenek T. 2000, *Nature*, 407, 349
- Ghez, A., et al. 2003, *ApJ*, 586, L127
- Haller, J. W., Rieke, M. J., Rieke, G. H., Tamblyn, P., Close, L., & Melia, F. 1996, *ApJ*, 456, 194
- Hawley, S., & Balbus, S. A. 2002, *ApJ*, 573, 738
- Jackson, J. M., Geis, N., Genzel, R., Harris, A. I., Madden, S., Poglitsch, A., Stacey, G. J., & Townes, C. H. 1993, *ApJ*, 402, 173
- Krabbe, A., Genzel, R., Drapatz, S., & Rotaciuc, V. 1991, *ApJ*, 382, L19
- Krabbe, A., et al. 1995, *ApJ*, 447, L95
- Lacy, J. H., Achtermann, J. M., & Serabyn, E. 1991, *ApJ*, 380, L71
- Lebofsky, M. J., & Rieke, G. H. 1987, in *AIP Conf. 155, The Galactic Center*, ed. D. C. Backer (New York: AIP), 79
- Lee, H. M. 1994, in *The Nuclei of Normal Galaxies*, ed. R. Genzel & A. I. Harris (NATO ASI Ser. C, 445; Dordrecht: Kluwer), 335
- Lenzen, R., Hofmann, R., Bizenberger, P., & Tusche, A. 1998, *Proc. SPIE*, 3354, 606
- Levin, Y., & Beloborodov, A. M. 2003, *ApJ*, 590, L33
- Liu, S., & Melia, F. 2002, *ApJ*, 566, L77
- Lo, K. Y., & Claussen, M. J. 1983, *Nature*, 306, 647
- Lucy, L. B. 1974, *AJ*, 79, 745
- Maeder, A., & Meynet, G. 1994, *A&A*, 287, 803
- Markoff, S., Falcke, H., Yuan, F., & Biermann, P. L. 2001, *A&A*, 372, L25
- McGinn, M. T., Sellgren, K., Becklin, E. E., & Hall, D. N. B. 1989, *ApJ*, 338, 824
- Melia, F. 1992, *ApJ*, 387, L25
- Melia, F., & Falcke, H. 2001, *ARA&A*, 39, 309
- Mezger, P. G., Duschl, W. J., & Zylka, R. 1996, *A&A Rev.*, 7, 289
- Morris, M. 1993, *ApJ*, 408, 496
- Morris, M., & Serabyn, E. 1996, *ARA&A*, 34, 645
- Murphy, B. W., Cohn, H. N., & Durisen, R. H. 1991, *ApJ*, 370, 60
- Najarro, F., Krabbe, A., Genzel, R., Lutz, D., Kudritzki, R. P., & Hillier, D. J. 1997, *A&A*, 325, 700
- Narayan, R., Yi, I., & Mahadevan, R. 1995, *Nature*, 374, 623
- Nayakshin, S., Cuadra, J., & Sunyaev, R. 2003, *A&A*, in press
- Ott, T., Eckart, A., & Genzel, R. 1999, *ApJ*, 523, 248
- Paumard, T., Maillard, J. P., Morris, M., & Rigaut, F. 2001, *A&A*, 366, 466
- Portegies Zwart, S. F., McMillan, S. L. W., & Gerhard, O. 2003, *ApJ*, in press
- Raab, W. 2002, Ph.D. thesis, Ludwig-Maximilians Universität München
- Rasio, F. A., & Shapiro, S. L. 1990, *ApJ*, 354, 201
- Reid, M. J. 1993, *ARA&A*, 31, 345
- Reid, M. J., Menten, K. M., Genzel, R., Ott, T., Schödel, R., & Brunthaler, A. 2003a, *Astron. Nachr.*, 324(S1), 3
- Reid, M. J., Menten, K. M., Genzel, R., Ott, T., Schödel, R., & Eckart, A. 2003b, *ApJ*, 587, 208
- Reid, M. J., Readhead, A. C. S., Vermeulen, R. C., & Treuhaft, R. 1999, *ApJ*, 524, 816
- Rieke, G. H., & Rieke, M. J. 1994, in *The Nuclei of Normal Galaxies*, ed. R. Genzel & A. I. Harris (NATO ASI Ser. C, 445; Dordrecht: Kluwer), 283
- Rieke, G. H., Rieke, M. J., & Paul, A. E. 1989, *ApJ*, 336, 752
- Rousset, G., et al. 1998, *Proc. SPIE*, 3353, 508
- Schödel, R., et al. 2002, *Nature*, 419, 694
- , 2003, *ApJ*, submitted
- Scoville, N. Z., & Kwan, J. 1976, *ApJ*, 206, 718
- Scoville, N. Z., Stolovy, S., Rieke, M., Christopher, M., & Yusef-Zadeh, F. 2003, *ApJ*, in press
- Sellgren, K., McGinn, M. T., Becklin, E. E., & Hall, D. N. B. 1990, *ApJ*, 359, 112
- Shara, M., Saffer, R., & Livio, M. 1997, *ApJ*, 489, L59
- Sills, A., & Bailyn, C. D. 1999, *ApJ*, 513, 428
- Sills, A., Faber, J. A., Lombardi, J. C., Jr., Rasio, F. A., & Warre, A. R. 2001, *ApJ*, 548, 323
- Tamblyn, P., Rieke, G. H., Hanson, M. M., Close, L. M., McCarthy, D. W., & Rieke, M. J. 1996, *ApJ*, 456, 206
- Tanner, A., Ghez, A., Morris, M., Becklin, E., Cotera, A., Ressler, M., Werner, M. W., & Wizinovich, P. 2002, *ApJ*, 575, 860
- Thorne, K. S., & Zytzkow, A. N. 1975, *ApJ*, 199, L19
- Tiede, G. P., Frogel, J. A., & Terndrup, D. M. 1995, *AJ*, 110, 2788
- Vollmer, B., & Duschl, W. 2000, *NewA*, 4, 581
- Young, P. 1980, *ApJ*, 242, 1232
- Yusef-Zadeh, F., Roberts, D. A., & Biretta, J. 1998, *ApJ*, 499, L159
- Zhao, J. H., & Goss, W. M. 1998, *ApJ*, 499, L163
- , 1999, in *ASP Conf. Ser. 186, The Central Parsecs of the Galaxy*, ed. H. Falcke, A. Cotera, W. J. Duschl, F. Melia, & M. J. Rieke (San Francisco: ASP), 224
- Zoccali, M., et al. 2003, *A&A*, 399, 931